Correlation Between Microstructure and Mechanical Property Evolution in Ferritic-Martensitic and Oxide Dispersion-Strengthened Alloys

A Thesis
Presented in Partial Fulfillment of the Requirements for the
Degree of Master of Science
with a
Major in Mechanical Engineering
in the
College of Graduate Studies
University of Idaho
by
Maxwell J. Johnson

Major Professor: Matthew Swenson, Ph.D.
Committee Members: Michael Maughan, Ph.D.; Steven Beyerlein, Ph.D.
Department Administrator: Gabriel Potirniche, Ph.D.

August 2021

Authorization to Submit Thesis

This thesis of Maxwell J. Johnson, submitted for the degree of Master of Science with a Major in Mechanical Engineering and titled "Correlation Between Microstructure and Mechanical Property Evolution in Ferritic-Martensitic and Oxide Dispersion-Strengthened Alloys," has been reviewed in final form. Permission, as indicated by the signatures and dates below, is now granted to submit final copies to the College of Graduate Studies for approval.

Major Professor: _____ Date: _____
Matthew Swenson, Ph.D.

Committee Members: _____ Date: _____
Michael Maughan, Ph.D.

_____ Date: _____
Steven Beyerlein, Ph.D.

Department Administrator: _____ Date: _____
Gabriel Potirniche, Ph.D.

Abstract

With the rising global demand for low-cost clean energy, nuclear fission and fusion systems will become increasingly important sources for both economic and environmental reasons. These new advanced systems will operate at a higher efficiency compared to previous models. This will require materials to be long-lasting durable and have excellent high-temperature performance (up to 700°C) under adverse conditions. Qualities such as resistance to oxidation, resistance to swelling, and low levels of radioactivation will be critical for any material used in nuclear reactor components, specifically for fuel cladding or structural elements surrounding the reactor core. Materials research historically focused on austenitic stainless steels, superalloys, or ferritic-martensitic (F-M) steels. Chapter 2 of this study focuses on three FM steels, HT-9, HCM12A, and T91In order to understand the effects of irradiation, charged particle irradiation is used to imitate the damage on these candidate materials. To better understand the effects of irradiation, the dispersed barrier hardening model was coupled with the solid solution strengthening model. These models are used to quantify the strengthening caused by irradiation induced micro-, and nano-structure features. Chapter 3 of this study focuses on one ODS alloy, MA956. A similar approach was taken to understand the effects of irradiation-induced micro-, and nano-structure features, as well as the effects of friction stir welding on the material. To better understand these effects, the dispersed barrier hardening model was coupled with the solid solution strengthening model and the grain size dependence (Hall-Petch) model. Coupled with nanoindentation, transmission electron microscopy (TEM), and atom probe tomography (APT), irradiation induced, and friction stir welding features can be numericized, and evaluated on the significant changes they contribute to the overall change in strength of the material These two chapters are intended to be inserts of two separate manuscript publications.

Acknowledgements

I would like to express great gratitude towards my major professor and mentor Dr. Matthew Swenson. His support, guidance, patience, and advice on this project have been non the less but amazing. I could not ask for a better experience overall. I would also like to thank my committee members, Dr. Michael Maughan, and Dr. Steven Beyerlein as well. Their great insight along the way has only been beneficial in making this thesis what it is.

Thanks to all the professors, factuality, and staff at the University of Idaho for providing me with the great educational opportunities and experiences along the way.

Also, thanks to all my fellow graduate, and undergraduate students that I have had the pleasure with working and studying alongside with during this journey.

Dedication

This thesis is dedicated to all my family and friends that have made this process as great as it has been. Special thanks to my father, Tim, my mother, Kim, and my sister Kacy for always supporting my decisions throughout this time.

Table of Contents

List of Tables

List of Figures

Statement of Contribution

In Chapter 1 of this thesis is a manuscript that is in the process of being published. It was a collaborative effort with my advisor, Dr. Matthew Swenson, and myself. The nanoindentation data of the HT9 was conducted by Matthew Harned at KLA-Tencor and is also present in his thesis. In Chapter 2 of this thesis are sections that are intended to be used for another manuscript that will be published with Dr. Elizabeth Getto at the Naval Academy, and my advisor Dr. Matthew Swenson. The writing in this thesis was completed by me and reviewed by Dr. Matthew Swenson.

Chapter 1: Introduction

With the rising global demand for a low-cost clean energy source, an international forum set out to determine how they could accomplish this. Within that forum Generation IV nuclear reactor designs were presented. The leading design currently is a sodium fast cooled reactor (SFR) which uses liquid sodium to cool the fuel source. These new advanced systems will operate at a much higher efficiency than previous models. The goal is to create an energy system that will be highly economical, extremely safe, and emulate a closed fuel cycle creating as little waste as possible while producing as much power as possible. While these new advanced systems will operate at a much higher efficiency this means that they will require more advanced materials to withstand these conditions. The materials are required to withstand temperatures of up to 700°C as well as adverse conditions. They will need to be longer lasting, and more durable than previous materials, and will need to be resistant to oxidation, swelling, and radioactivation. Ferritic-martensitic, and oxide dispersion-strengthening alloys are both candidate materials for in core applications, and structural elements in nuclear fission reactors.

Heavy ion and proton irradiation are used to emulate the effects of neutron irradiation. This method reduces the irradiation time and allows the materials to be safe to handle. It is an accepted method to study irradiation-induced micro-, and nano- structure features. Using heavy ion and proton irradiation creates some challenges. Upon irradiation only a thin irradiated film occurs on the sample. Nanoindentation is needed to sample the irradiated region. If other indentation methods were used, they would sample too deep into the surface, and it would not provide accurate results. Irradiation induced microstructure features, and ODS alloy features, including dislocation loops, nanoclusters, voids, and dispersoids were all characterized in previous studies to determine the size and density present in the material. That information was leveraged in this study to complete a model that can compare the irradiation induced microstructure features to the change in yield strength of the material.

Previous studies on these advanced materials have typically used TEM to characterize the microstructure and coupled it with the dispersed barrier hardening to create a simple correlation between the effects of irradiation-induced microstructure features and the change in yield strength of the material. However, in this approach it often lacks information relating the solute migration, and solute clustering from irradiation.

The objective of this study is to create a model that combines the dispersed barrier hardening model, solid solution strengthening model, and the grain size dependence (Hall-Petch) model to create a comprehensive correlation to the change in yield strength resulting from irradiation induced microstructure evolution and friction stir welding effects. In chapter 2 of this study three commercial grade ferritic-martensitic alloys, HT9, HCM12A, and T91 are irradiated with heavy ions and protons. Nanoindentation is used to determine the change in yield strength due to irradiation. TEM and APT characteristics from previous studies are implemented into the dispersed barrier hardening model, and the solid solution strengthening model to quantify these characteristics and determine the change in yield strength from irradiation-induced. In chapter 3 of this study, a commercial grade oxide dispersion-strengthened alloy, MA956 is irradiated with heavy ions. TEM, APT, EBSD, and SEM were all characterized in previous studies and leveraged in the dispersed barrier hardening model, solid solution strengthening model, and grain size dependence (Hall-Petch) model to determine the change in yield strength as a result of irradiation-induced microstructure features as well as the effects of friction stir welding on ODS alloy, MA956.

Chapter 2: Irradiation-induced solute migration and clustering effects on mechanical properties in ferritic-martensitic alloys

Abstract

The objective of this study is to evaluate and numericize the effects of irradiation induced hardening on Ferritic/Martensitic (F/M) alloys using the dispersed barrier hardening (DBH) on three commercial alloys HT9, HCM12A, and T91. We present a large data set spanning the three alloys including irradiations at 3 dislocations per atom (dpa), 100 dpa, and 2.4 dpa proton. All alloys were irradiated at 500 °C. Nanoindentation was performed on all samples to determine the change in hardness as a result of irradiation. Nanoclusters were characterized using Atom probe tomography (APT) pre and post irradiation. Microscopic level defects were characterized using transmission electron microscopy (TEM). Nanocluster solute sizes were combined to create an overall effective diameter and was discovered to be a feasible way to evaluate in the DBH model. It was concluded that nanoclusters in the matrix act coherently and cannot be considered negligible when determining the increase in strength due to irradiation.

Introduction

With rising global demand for low-cost clean energy, nuclear fission and fusion systems will become increasingly important energy sources for both economic and environmental reasons. Advanced systems will operate at higher efficiency, requiring materials to be long-lasting and durable, and have excellent high-temperature performance (up to 700°C) under adverse conditions (several hundred dpa). [1–3] Qualities such as resistance to oxidation, resistance to swelling, and low levels of radioactivation will be critical for any material used

in nuclear reactor components, specifically fuel cladding or structural elements surrounding the reactor core. Materials research has historically focused on austenitic stainless steels, superalloys, or ferritic-martensitic (F-M) steels. Three alloys of the latter category, HT-9, HCM12A, and T91, are the subjects of this study.

While these materials are candidate materials for advanced fission reactors that experience high doses of neutron irradiation, the materials in this study were irradiated using charged particle irradiation. Charged particle irradiation is used to accelerate the irradiation effects on the alloys, due to the timely process of neutron irradiation. Although the processes differ, charged particle irradiation has been a widely accepted method to emulate the irradiation effects on alloys. Neutron irradiation experiments are extremely time consuming, expensive, and the materials are activated, and only able to be processed within advanced laboratories. Charged particle irradiation can be concluded within hours or days, and typically causes no activation of the material.

Although ion irradiation is extremely beneficial in accelerating the effects of neutron irradiation, it makes testing mechanical properties much more challenging. With ion irradiation, the damaged layer of material is very shallow (1-10 μm). Traditional methods of mechanical testing will not target the irradiated zone, and will sample properties of the base material giving imprecise results [4,5]. Nanoindentation is simple small scale method that can accurately measure the mechanical properties of the irradiated material layer [6,7].

In order to better understand the effects of irradiation the dispersed barrier hardening (DBH) model is used to analyze and quantify the microstructure features in the matrix. Through previous studies on F-M steels and other alloys it was found that the DBH model is an excellent model to determine the strengthening factors of each microstructure feature. [8–

10]. While the DBH model offers a great understanding of how microstructure features apply to the overall strength of the material, it cannot be applied simultaneously to all radiation conditions. Kotrechko et al. [11] verified the model using raised temperature control experiments in RPV alloys. As temperature was increased strengthening coefficients for loops and precipitates decreased. This trend is promising, as it agrees with common belief on microstructure defects at elevated temperatures. All though there are many studies that have included the DBH model, there is a very much needed gap to fill. The exploration of high dose, and the understanding on how nanoclusters react amongst each other within a variety of F-M steels can do so.

In the three F-M alloys presented in this study, the focus on nanoclusters is key. Through the use of atom probe tomography, it was deduced that upon irradiation Si-Mn-Ni, and Cu nanoclusters are developed, and are understood to be a key strengthening factor in the material. Schaublin et al. [12] note that irradiation induced hardening of F/M steels is hard to rationalize in terms of the damage observed in TEM, which adds to why atom probe tomography is beneficial to include. Though this is very important information, what is misunderstood is how the nanoclusters react with each other. In this study, it is assumed that all Si-Mn-Ni nanoclusters combined with Cu clusters creating a much larger overall cluster. The remaining copper clusters are considered in the overall effective diameter of each cluster to simplify the DBH model. This simply allows to solve for the strengthening coefficient of nanoclusters as a whole, and better represent the microfeature.

The objective of this study is to apply an analytic model combining dispersed barrier hardening and solid solution strengthening mechanisms to relate microstructure and microchemistry in three irradiated F/M alloys (HT9, HCM12A, and T91) to their respective

mechanical hardness. The study will accomplish this through evaluation of solute migration resulting from irradiation at 500 °C with either 2 MeV protons, or 5 MeV Fe^{2+} ions to doses ranging 1 - 100 dpa and the combination of nanoindentation with previously measured microstructures on a subset of these specimens. Multiple approaches for superimposing the effects of dispersed barriers and solid solution strengthening are considered, and the strengthening factors for dispersed barriers are estimated using a deductive approach enabled by nanoindentation across specimens with varied irradiation-induced features in their microstructure.

Experiments

Material, irradiations, and microscopy

The work in this study focuses on three commercial F/M alloys. Alloy HT9 (nominally 12CR-MoVW) was austenitized at 1040°C for 30 minutes followed by air cooling, then tempered at 760°C for 60 minutes followed by air cooling to room temperature to produce a three-phase microstructure of martensite, δ-ferrite, and retained austenite. Alloy HCM12A (nominally 12Cr-MoVNbWCu), was austenitized at 1050°C for 60 minutes followed by air cooling, then tempered at 770°C for 45 minutes followed by air cooling to room temperature. This resulted in a two-phase microstructure comprised of martensite laths, and δ-ferrite needles. Alloy T91 (nominally 9Cr-MoVNb) was austenitized at 1040°C for 1 hour followed by air-cooling, then tempered at 760 C for 60 minutes followed by air cooling to room temperature. This has primarily a martensitic structure with small laths. Chemical compositions for each alloy are provided in Table 1.1.

Table 2.1 Chemical composition of commercial F/M alloys HT9, HCM12A, and T91 (at%) [13,14].

Element	HT9	HCM12A	T91
Cr	12.34	11.62	8.91
C	0.92	0.51	0.46
Si	0.43	0.54	0.55
Mn	0.52	0.65	0.45
Ni	0.47	0.37	0.20
Cu	0.035	0.90	0.15
W	0.16	0.57	-
V	0.32	0.21	0.23
Nb	-	0.032	0.05
Mo	0.58	0.17	0.52
N	0.19	0.25	0.19
P	0.036	0.029	0.016
Al	<0.02	0.002	0.045
S	0.010	0.003	0.005
Ti	0.002	-	-
O	0.045	-	-
Fe	Bal.	Bal.	Bal.

Specimens were prepared from the same heats of each alloy for multiple irradiations at the Michigan Ion Beam Laboratory. The primary focus of this study is on two separate irradiations with 5 MeV Fe^{2+} self-ions (~2.2 x 10^{-4} dpa/s) to doses of 3 displacements per atom (dpa) and 100 dpa, respectively, for each alloy. In addition, a sample of HCM12A irradiated with 2 MeV protons (~1.1 x 10^{-5} dpa/s) to 2.4 dpa were evaluated for comparison. All irradiations were conducted at 500 °C. The damage profiles for each charged particle irradiation were estimated using the Stopping and Range of Ions in Matter (SRIM) software [15] A summary of the irradiation conditions evaluated and the corresponding characterization in this study is provided in Table 1.2 The specimens analyzed were part of the same irradiation campaign found in Refs. [13,14,16]

Table 2.2. Summary of irradiation conditions evaluated in this study. All irradiations were conducted at 500 °C.

Alloy	**2 MeV protons (1.2×10^{-5} dpa/s)**	**5 MeV Fe^{2+} ions (2.2×10^{-4} dpa/s)**	
	2.4 dpa	**3 dpa**	**100 dpa**
HT9	-	[13,16]	-
HCM12A	[13,16]	[13,16]	[13,16]
T91	-	[14]	[14]

Transmission electron microscopy (TEM) analysis of each specimen was conducted to evaluate the microstructure evolution under heavy ion (or proton) irradiation. TEM lamellae were prepared from the as received and irradiated specimens using conventional focused ion beam (FIB) techniques on an FEI Quanta 3D FEG FIB at the Center for Advanced Energy Studies (CAES). All details regarding TEM sample preparation and analysis are found in refs. [14,16]

Atom Probe Tomography (APT) complemented the TEM analysis to evaluate any nanoscale clustering of solutes and the solute chemistry of the matrix following each irradiation. APT needles were fabricated using conventional FIB milling techniques from each irradiated specimen at CAES and analyzed using a LEAP 4000X HR, as detailed in refs. [13,14] Cluster analysis was performed on each sample needle (excluding volumes intersecting grain boundaries and carbide precipitates) using the maximum separation method [17] within the Integrated Visualization and Analysis Software (IVAS). Matrix concentrations were also derived from the cluster analysis results, even for samples that did not contain any irradiation-induced clusters.

Nanoindentation

Nanoindentation was conducted on each specimen to understand and assess the hardness changes between the as received and irradiated specimens of each alloy. Two main approaches are used to find the modulus and hardness during a nanoindentation test: continuous stiffness measurement (CSM) and quasi-static stiffness measurement. In the CSM technique, the indenter tip is oscillated at a sufficiently high frequency (often 40Hz) to retrieve the force/displacement measurements continuously while progressively increasing the load to drive the tip into the material, giving a complete hardness vs. depth profile. This approach has the advantage of being able to continuously measure the hardness at every depth, rather than at a discrete set of points, giving a fuller picture of the material properties as a function of depth. There is evidence, however, that the oscillation of the tip in the material produces a change in the material itself; the alloy can strain-harden or soften under the variable load [18,19]. With quasi-static testing, the indenter head penetrates and holds, then measures the elastic stiffness on retraction. This gives only discrete points at which the properties are known, but it avoids any issues arising from the application of a harmonic stress to the material. In this study, quasi-static nanoindentation was used rather than CSM. Nanoindentation of each specimen (using the quasi-static method) was conducted using a KLA-Tencor G200 nano-indenter. A surface detection threshold stiffness of 200 N/m was used; this parameter is used to identify when the tip contacts the sample surface. If this threshold is set too low, signal noise may cause it to identify surface contact too early and, if set too high, the tip will indent the surface before data collection begins. In either case, the displacement will be misreported, and the modulus and hardness data may be skewed. Tip calibration was done using a sample of fused silica as a standard; a 2nd-order polynomial

area function was fitted, and analysis was done in the NanoSuite software using the Oliver-Pharr method [20].

Measurements for each of the HT9 samples was completed at KLA-Tencor in Milpitas, CA using a load-controlled approach. Meanwhile, measurements on the T91 and HCM12A samples was conducted at the University of Idaho, in Moscow, ID. using a displacement-controlled method. Both techniques were conducted using a Berkovich diamond tip indenter. Samples were prepared for indentation by using mounting wax to adhere them to a glass bed which was mounted to an aluminum puck. The indentations were made into the irradiated surface (oriented parallel to the irradiating beam) using the G200 instrument and the "Basic Method." Each sample was indented at 15-25 different locations, spaced at least 25-60 μm apart to avoid plastic zone interference since the plastic zone of each indent is expected to be ~4-5 times deeper than the indent itself [21–26]. The tip was loaded and unloaded at 10-20 depths per indent site, with progressively more unloading at greater depths. Each indentation load cycle included a 15-second load time and a 10-second hold at maximum load, followed by a 90% unload. From each indent location, the average depth was determined for each loading/unloading point within the indents, and an average hardness at each depth was calculated, along with a standard deviation and the standard deviation of the mean for both the depth and hardness values.

Results

Transmission electron microscopy

The microstructures for each of the three alloys were characterized using TEM imagining of the as received and each irradiated specimen. A summary of the microstructure measurements is summarized in Table 1.3 Average grain sizes in the HT9 alloy were slightly smaller (ranging 0.38 – 0.41 μm) than the HCM12A and T91 alloys which had average sizes ranging 0.59 – 0.63 μm, but none of the grains in each alloy were found to be modified substantially following any of the irradiations. Similarly, dislocation line densities range 12.1 x 10^{14} m^{-2} to 14.6 x 10^{14} m^{-2} in HT9 and HCM12A and are slightly higher in T91 with a range of 13.9 x 10^{14} m^{-2} to 17.2 x 10^{14} m^{-2}. But these measurements carry wide standard deviations, suggesting that dislocation line density has not been altered dramatically during irradiation. The observed carbide precipitates in all three alloys are comparable in size ranging 0.07 - 0.11 μm and are also not found to dramatically evolve upon irradiation. The number density of carbides appears to be slightly higher in HT9 (0.62 – 0.70 x 10^{20} m^{-3}) than in HCM12A (0.22 – 0.53 x 10^{20} m^{-3}) and T91 (0.37 – 0.61 x 10^{20} m^{-3}), which is consistent with the higher concentrations of C and Cr in the HT9 alloy (Table 1.1).

Voids are only observed in HCM12A following irradiation to 100 dpa. The HCM12A sample irradiated with Fe^{2+} ions to 100 dpa exhibits a low density of voids (0.2 ± 0.2 x 10^{21} m^{-3}) with average diameter of 6.1 ± 5.4 nm. Meanwhile, all the irradiated specimens exhibit dislocation loops. Following irradiation to 2.4 – 3.0 dpa, the average size of loops in HT9 and HCM12A (7.6 – 7.7 μm) are almost identical, while number densities are also reasonably consistent (2.0 – 4.4 x 10^{21} m^{-3}). Loops following 3 dpa irradiation in T91 appear to be slightly coarser with size and number density at 10.4 ± 3.6 nm and 0.6 ± 0.1 x 10^{21} m^{-3},

respectively. When Fe^{2+} irradiation increased to 100 dpa in HCM12A, the loops appear to coarsen to slightly larger size and lower number density of 12.0 ± 4.5 nm and 1.0 ± 0.2 x 10^{21} m^{-3}, respectively. Meanwhile, after 100 dpa irradiation in T91, loops are even larger at 13.2 ± 3.9 nm and density appears to be slightly higher at 1.6 ± 0.7 x 10^{21} m^{-3}.

Table 2.3. Summary of microstructure measurements using TEM. Errors are reported as the standard deviation.

Feature	Measurement	**HT9** [16]		**HCM12A** [16]				**T91** [14]		
		As received	**Fe^{2+} ion-irradiated (3 dpa, 500 °C)**	**As received**	**Proton-irradiated (2.4 dpa, 500 °C)**	**Fe^{2+} ion-irradiated (3 dpa, 500 °C)**	**Fe^{2+} ion-irradiated (100 dpa, 500 °C)**	**As received**	**Fe^{2+} ion-irradiated (3 dpa, 500 °C)**	**Fe^{2+} ion-irradiated (100 dpa, 500 °C)**
Grains/Laths	Effective diameter ($\times 10^{-6}$ m)	0.38 ± 0.11	0.41 ± 0.16	0.63 ± 0.13	0.61 ± 0.26	0.63 ±0.22	0.61 ± 0.18	0.59 ± 0.17	0.60 ± 0.12	0.61 ± 0.11
Dislocation lines	Density ($\times 10^{14}$ m^{-2})	12.4 ± 2.4	13.6 ± 12.6	12.3 ± 0.09	12.1 ± 4.2	13.3 ± 4.4	14.6 ± 1.9	13.9 ± 6.2	16.6 ± 6.6	17.2 ± 4.0
Carbide Precipitates	Effective diameter ($\times 10^{-6}$ m)	0.10 ± 0.03	0.07 ± 0.03	0.10 ± 0.03	0.11 ± 0.05	0.09 ± 0.04	0.11 ± 0.06	0.10 ± 0.04	0.08 ± 0.03	0.09 ± 0.04
	Density ($\times 10^{20}$ m^{-3})	0.70 ± 0.10	0.62 ± 0.28	0.37 ± 0.23	0.53 ± 0.28	0.35 ± 0.10	0.22 ± 0.11	0.53 ± 0.28	0.37 ± 0.12	0.61 ± 0.14
Voids	Average diameter ($\times 10^{-9}$ m)	-	-	-	-	-	6.1 ± 5.4	-	-	-
	Density ($\times 10^{21}$ m)	-	-	-	-	-	0.2 ± 0.2	-	-	-
Dislocation loops	Average diameter ($\times 10^{-9}$ m)	-	7.6 ± 2.3	-	7.6 ± 2.4	7.7 ± 2.4	12.0 ± 4.5	-	10.4 ± 3.6	13.2 ± 3.9
	Density ($\times 10^{21}$ m)	-	2.0 ± 0.3	-	4.4 ± 1.1	2.2 ± 0.3	1.0 ± 0.2	-	0.6 ± 0.1	1.6 ± 0.7

Atom probe tomography

To achieve an objective characterization of any irradiation-induced solute clustering, APT was used to quantify the average size and number density of nanoclusters as well as any changes to the solute matrix composition following each irradiation. A summary of the quantitative measurements using APT is provided in Table 1.4. In alloy HT9, there are not any Si-Mn-Ni-rich or Cu-rich irradiation-induced nanoclusters observed following Fe^{2+} irradiation to 3 dpa, but the combined matrix composition of Si, Mn, Ni, and Cu is 1.12 at%, and is lower than the nominal concentration of the same solutes (~1.46 at%) from Table 1.1.

In alloy HCM12A, irradiation-induced Si-Mn-Ni-rich and Cu-rich nanoclusters are observed following both proton irradiation to 2.4 dpa and Fe^{2+} irradiation to 3 dpa, often at adjacent locations. Interestingly, the Si-Mn-Ni-rich nanoclusters following proton irradiation (with average size of 9.63 ± 0.43 nm and density of 19 x 10^{21} m^{-3}) are significantly coarser than they are following Fe^{2+} irradiation to 3 dpa (average size of 5.95 ± 0.23 nm and density of 92 x 10^{21} m^{-3}). A similar trend is observed for the Cu-rich clusters as well, though the difference in clusters sizes (6.82 ± 0.32 nm and 6.18 ± 0.13 nm, respectively) is not as dramatic. The combined matrix composition of Si, Mn, Ni, and Cu following proton irradiation to 2.4 dpa and Fe^{2+} irradiation to 3 dpa are 1.39 at% and 1.64 at%, respectively, with the lower matrix composition following proton irradiation consistent with the higher volume fraction of nanoclusters observed. These values are also lower than the nominal concentration of the same solutes (~2.45 at%) from Table 1.1. No irradiation-induced nanoclusters are observed following Fe^{2+} irradiation to 100 dpa, but the matrix composition of Si, Mn, Ni, and Cu is further reduced to 1.15 at%.

In Alloy T91, Si-Mn-Ni-rich and Cu-rich nanoclusters are also observed following Fe^{2+} irradiation to 3 dpa at adjacent locations, but with lower density and volume fraction than HCM12A. Irradiation-induced Si-Mn-Ni-rich clusters have average size of 7.59 ± 0.53 nm and number density of 12 x 10^{21} m^{-3}, while Cu-rich clusters are at an average size of 7.54 ± 0.77 nm and density of 14 x 10^{21} m^{-3}. Similar to HCM12A, no irradiation-induced nanoclusters are found following Fe^{2+} irradiation to 100 dpa. Interestingly, the combined matrix compositions of Si, Mn, Ni, and Cu after irradiation to 3 dpa (1.33 at%) is very close to the nominal composition of the same solutes (~1.35 at%), consistent with the low volume fraction of clusters, and only slightly declines after 100 dpa to 1.26 at%.

Table 2.4. Summary of nanocluster characterization and matrix composition measurements using APT. Errors are reported as the standard deviation of the mean.

Feature	**HT9** [13]	**HCM12A** [13]			**T91** [14]	
	Fe^{2+} ions (3 dpa, 500 °C)	**Protons (2.4 dpa, 500 °C)**	**Fe^{2+} ions (3 dpa, 500 °C)**	**Fe^{2+} ions (100 dpa, 500 °C)**	**Fe^{2+} ions (3 dpa, 500 °C)**	**Fe^{2+} ions (100 dpa, 500 °C)**
Si-Mn-Ni-rich Nanoclusters						
Average Diameter, D_G^{SiMnNi} (nm)	-	9.63 ± 0.43	5.95 ± 0.23	-	7.59 ± 0.53	-
Number Density, N_{nc}^{SiMnNi} (x 10^{21} m^{-3})	-	19	92	-	12	-
Volume fraction, f_v^{SiMnNi}	-	1.89%	1.08%	-	0.48%	-
Cu-rich Nanoclusters						
Average Diameter, D_G^{Cu} (nm)	-	6.82 ± 0.32	6.18 ± 0.13	-	7.54 ± 0.77	-
Number Density, N_{nc}^{Cu} (x 10^{21} m^{-3})	-	19	107	-	14	-
Volume fraction, f_v^{Cu}	-	0.65%	0.52%	-	0.02%	-
Combined Effective Diameter, $D_G^{SiMnNiCu}$ (nm)	-	10.66	7.44	-	9.24	-
Combined Number Density, N_{comb} (x 10^{21} m^{-3})	-	19	107	-	14	-

Nanoindentation

Nanoindentation results for the as received and irradiated specimens for each alloy evaluated in this study are illustrated as a function of indentation depth in Fig. 1.1. At the shallower indentation depths (<400 nm) there is evidence of the indentation size effect resulting in a progressively increasing hardness at shallower depths [27] with wider error ranges due to the surface roughness. Meanwhile, it is expected that deeper indents will progressively sample more of the unirradiated substrate below the irradiated layer of the Fe^{2+} irradiated specimens, which is considered to be a thin film of ~1.8 μm thickness. Robertson and Fivel have previously found that mechanical properties for thin ion-irradiated layers can be isolated from the substrate at indentation depths of <1/3 or the thickness [28], which is ~600 nm for this study. Additional evidence to support this approach is observed in the nanoindentation results for HCM12A in Fig. 1.1b, in which the hardness of the as-received and proton-irradiated specimen (which has a much deeper damage thickness of ~20 μm) appears to plateau at depths greater than ~500 nm, while the hardness of the Fe^{2+} irradiated specimens continue to decline at these same depths. As a result, indents made between 400 – 575 nm deep for HT9 and 400-650 nm deep for HCM12A and T91 are considered to be the most representative of the hardness, as indicated in Fig. 1.1. Using these values, an overall average hardness and standard deviation of the mean is calculated to establish an estimated mean hardness for each specimen.

For the HT9 alloy, the nanohardness is estimated to be 3.32 ± 0.09 GPa, and 3.62 ± 0.05 GPa for the as-received and ion-irradiated (3 dpa), respectively. With a reasonably large quantity of indents, the ranges for the standard deviation of the mean values are narrow enough to indicate that the irradiated specimen is clearly harder than the as-received. For the

HCM12A alloy, the nanohardness of the as-received specimen is estimated to be 3.36 ± 0.07 GPa, while the nanohardness of the irradiated specimens are found to be 4.00 ± 0.03 GPa, 4.07 ± 0.03 GPa, 3.58 ± 0.04 GPa, following irradiated with protons (2.4 dpa), Fe^{2+} ions (3 dpa), and Fe^{2+} ions (100 dpa), respectively. Finally, in alloy T91, the nanohardness is estimated to be 3.16 ± 0.03 GPa, 3.42 ± 0.04 GPa, and 3.34 ± 0.030 GPa for the as-received, Fe^{2+} ion irradiated (3 dpa), and Fe^{2+} ion irradiated (100 dpa), respectively. Similar to the HCM12A alloy, T91 is found to demonstrate a higher hardness following 3 dpa irradiation with Fe^{2+} ions followed by a reduction in hardness and irradiation dose increases to 100 dpa (Fig. 1.1d).

Nanohardness measurements are particularly helpful for estimating the increase in yield strength as a result of ion irradiation. We can use the empirical relationship [29]:

$$\Delta\sigma_y = 3.06\Delta H_v \quad (1)$$

with $\Delta\sigma_y$ representing the increase in yield strength (in MPa) due to irradiation and ΔH_v as the measured increase in Vickers hardness (in kg/mm^2). In this case, we use the relationship developed by Fischer-Cripps to convert Berkovich hardness (in GPa) into Vickers hardness (in kg/mm^2) via $H_V = 94.495H_{Berk}$ [30]. Following this approach, the change in yield strength for the HT9 alloy is estimated to be 92 MPa following Fe^{2+} irradiated to 3 dpa. In the HCM12A alloy, yield strength increase is found to be 201 MPa, 222 MPa, and 70 MPa following proton irradiation (2.4 dpa), Fe^{2+} ion irradiation to 3 dpa, and Fe^{2+} ion irradiation to 100 dpa, respectively. For the T91 alloy, yield strength increase is 82 MPa and 55 MPa following ion irradiation the 3 dpa and 100 dpa, respectively.

A complete summary of the estimated nanohardness values and increases in hardness and yield strength for the irradiated specimens is provided in Table 1.5. These results are consistent with archival literature. Allen et al. [31] note an increase of 0.15 GPa in HCM12A when irradiated with protons to 3 dpa at 500°C, and 0.49 GPa when irradiated to 10 dpa at 400°C. Wharry et al. [32] describe an increase in hardness in T91 of 0.24 GPa after a 3 dpa proton irradiation dose at 400°C. Krumwiede et al. [33] found that after an exposure to heavy ion irradiation to a dose of 6.49 dpa at 320°C, alloy T91 hardened by 0.99 GPa, and HT9 hardened by 1.45 GPa. Gao et al. [34] found the hardening of reduced activation martensitic steel F82H under Fe^{3+} irradiation to 30 dpa at 300°C to be 0.85 GPa. Zeman et al. [35] reports a hardening in T91 under 3.5 dpa proton irradiation (120°C) of about 0.116 GPa. Zhang et al. [36] observed an increase of about 0.163 GPa in a 9Cr-2W steel alloy, and 0.217 GPa in a similar alloy with the addition of 0.1 wt% Si after a 0.1 dpa neutron irradiation. Kareer et al. (Fe^{2+} Ions 452°C) [4], and Tan et al. (Neutron irradiated 469°C) [9] found an increase in hardness of T91 at low dose (1-5 dpa). Davis et al. (Fe^{4+} Ions 301-311°C) [37] found and increase in hardness of 13.1% and 21.4% in T91 at doses that range from 1.76 dpa – 4.10 dpa.

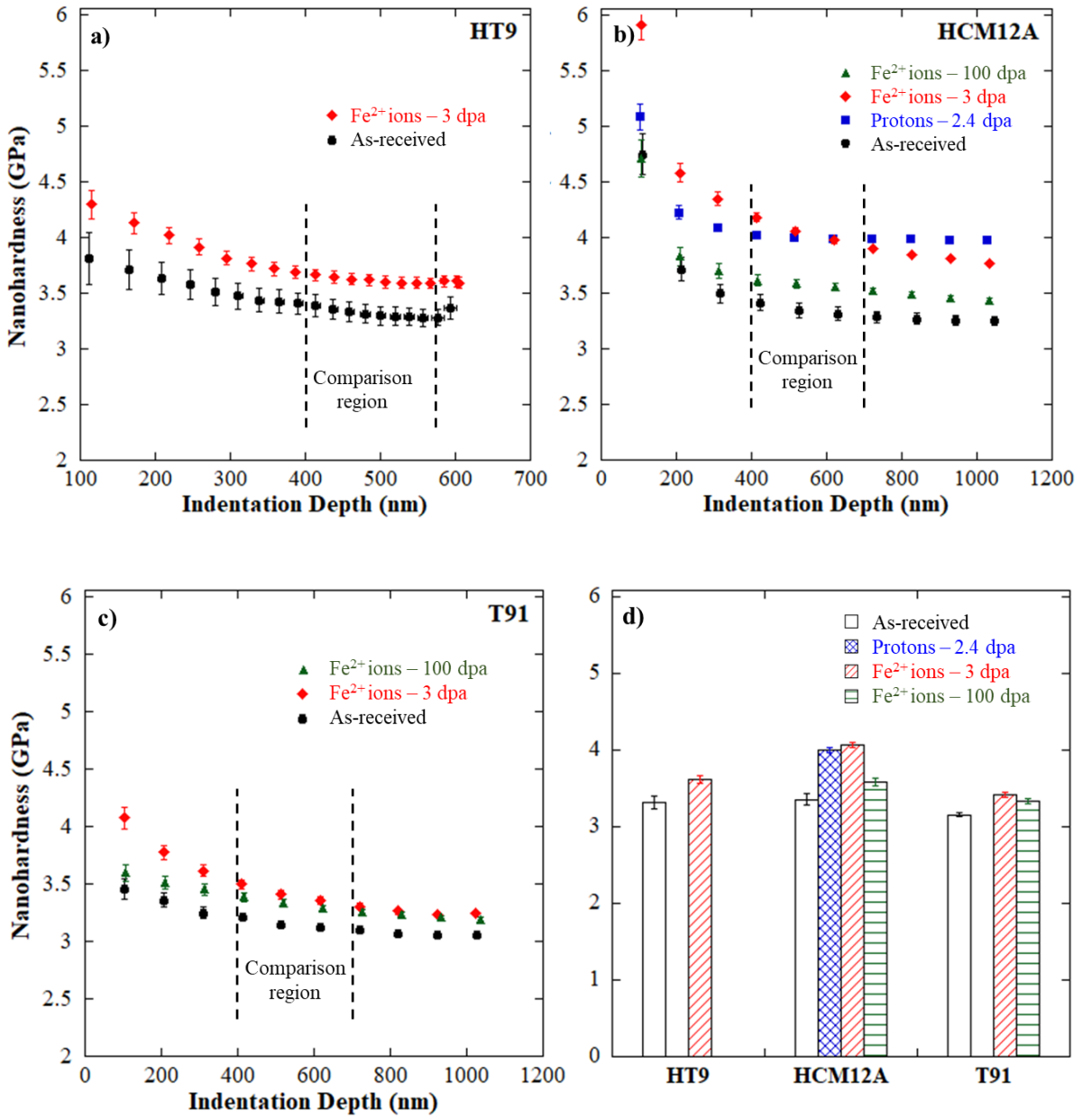

Figure 2.1. Nanoindentation hardness measurements via indentation parallel to the irradiation beam at various depths in irradiated F/M alloys: a) HT9, b) HCM12A, and c) T91. Estimated nanohardness values for each alloy are summarized in d).

Table 2.5. Summary of nanohardness measurements and estimated increase in hardness and yield strength for irradiated specimens.

Properties	HT9		HCM12A				T91		
	As received	**Fe^{2+} ion-irradiated (3 dpa, 500 °C)**	**As received**	**Proton-irradiated (2.4 dpa, 500 °C)**	**Fe^{2+} ion-irradiated (3 dpa, 500 °C)**	**Fe^{2+} ion-irradiated (100 dpa, 500 °C)**	**As received**	**Fe^{2+} ion-irradiated (3 dpa, 500 °C)**	**Fe^{2+} ion-irradiated (100 dpa, 500 °C)**
Nanohardness, H_{Berk} (GPa)	3.32 ± 0.09	3.62 ± 0.05	3.36 ± 0.07	4.00 ± 0.03	4.07 ± 0.03	3.59 ± 0.04	3.16 ± 0.03	3.42 ± 0.04	3.34 ± 0.03
Nanohardness increase, ΔH_{Berk}	-	0.30	-	0.64	0.71	0.23	-	0.26	0.18
Yield strength above as received, $\Delta\sigma_y$ (MPa)	-	86	-	186	206	65	-	76	51

Discussion

Solute migration

Following each of the irradiation conditions outlined in Table 1.2, the combined matrix compositions of solutes Si, Mn, Ni, and Cu appear to decline with higher irradiation dose. To further evaluate the evolution of matrix composition, solute concentration data from each of the irradiation experiments in ref. [13] are tabulated and illustrated in Table 1.6 and in Fig. 1.2, respectively, along with comparisons to the nominal bulk compositions in Table 1.1. With these additional irradiation conditions considered, the trend is further observed that solute matrix concentrations consistently declines with irradiation dose, but also appear to decline with irradiation duration, given that proton (~10^{-5} dpa/s) and neutron (~10^{-7} dpa/s) irradiation have progressively lower dose rates than Fe^{2+} irradiation (~10^{-4} dpa/s). The observed clustering behavior summarized in Table 1.4 is also likely closely tied to these respective concentration levels.

Table 2.6. Summary of matrix compositions for solutes Si, Mn, Ni, and Cu measured via APT for all irradiation conditions published in reference [13,14].

Alloy	Irradiation Condition	Matrix Compositions (at%)				
		Si	Mn	Ni	Cu	Si+Mn+Ni+Cu
HT9	Nominal (Table 1.1)	0.43	0.52	0.47	0.035	1.46
	p^+ (1 dpa)	0.26	0.58	0.23	0.08	1.15
	p^+ (2.4 dpa)	0.17	0.53	0.21	0.15	1.06
	Neutrons (3 dpa)	0.12	0.43	0.27	0.16	0.98
	Fe^{2+} (3 dpa)	0.26	0.65	0.15	0.06	1.12
	Fe^{2+} (100 dpa)	0.03	0.47	0.08	0.05	0.64
HCM12A	Nominal (Table 1.1)	0.54	0.65	0.37	0.90	2.45
	p^+ (1 dpa)	0.61	0.65	0.16	0.20	1.62
	p^+ (2.4 dpa)	0.48	0.62	0.13	0.16	1.39
	Neutrons (3 dpa)	0.43	0.54	0.09	0.16	1.22
	Fe^{2+} (3 dpa)	0.55	0.67	0.21	0.21	1.64
	Fe^{2+} (100 dpa)	0.30	0.69	0.04	0.12	1.15
T91	Nominal (Table 1.1)	0.55	0.45	0.20	0.15	1.35
	Neutrons (3 dpa)	0.40	0.40	0.07	0.10	0.98
	Fe^{2+} (3 dpa)	0.59	0.44	0.17	0.14	1.33
	Fe^{2+} (100 dpa)	0.56	0.48	0.09	0.13	1.26

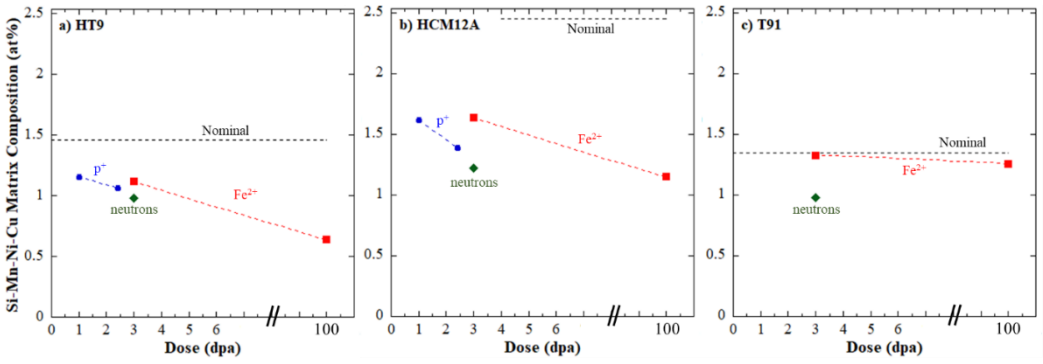

Figure 2.2. Combined matrix compositions for Si, Mn, Ni, and Cu following various irradiations in a) HT9, b) HCM12A, and c) T91 from ref. [13,14]. Matrix compositions of these solutes appear to decline with increasing dose and longer irradiation durations.

Of the three F/M alloys evaluated in this study, HT9 contains the lowest levels of Cu solutes. Since Cu is known to have a low solubility limit in b.c.c. Fe-based alloys, it is expected to precipitate quickly upon irradiation, providing nucleation sites for potential segregation and clustering of other solutes such as Si, Mn, and Ni [38]. At the same time, HT9 has the highest levels of Cr and C (resulting in a higher density of carbides) and the smallest grains of the three F/M alloys (Table 1.3), thus increasing the overall sink strength of HT9. This combined lack of Cu clustering and the presence of more numerous sinks for solutes to segregate to may explain why there are no Cu-rich or Si-Mn-Ni-rich nanoclusters following Fe^{2+} irradiation to 3 dpa, unlike the other F/M alloys in this study. In fact, through evaluation of the LEAP samples for HT9 following each irradiation in ref. [13], several examples of sink segregation are visibly present, demonstrating solute segregation to grain boundaries, carbide precipitates, and VN-based precipitates (Fig. 1.3).

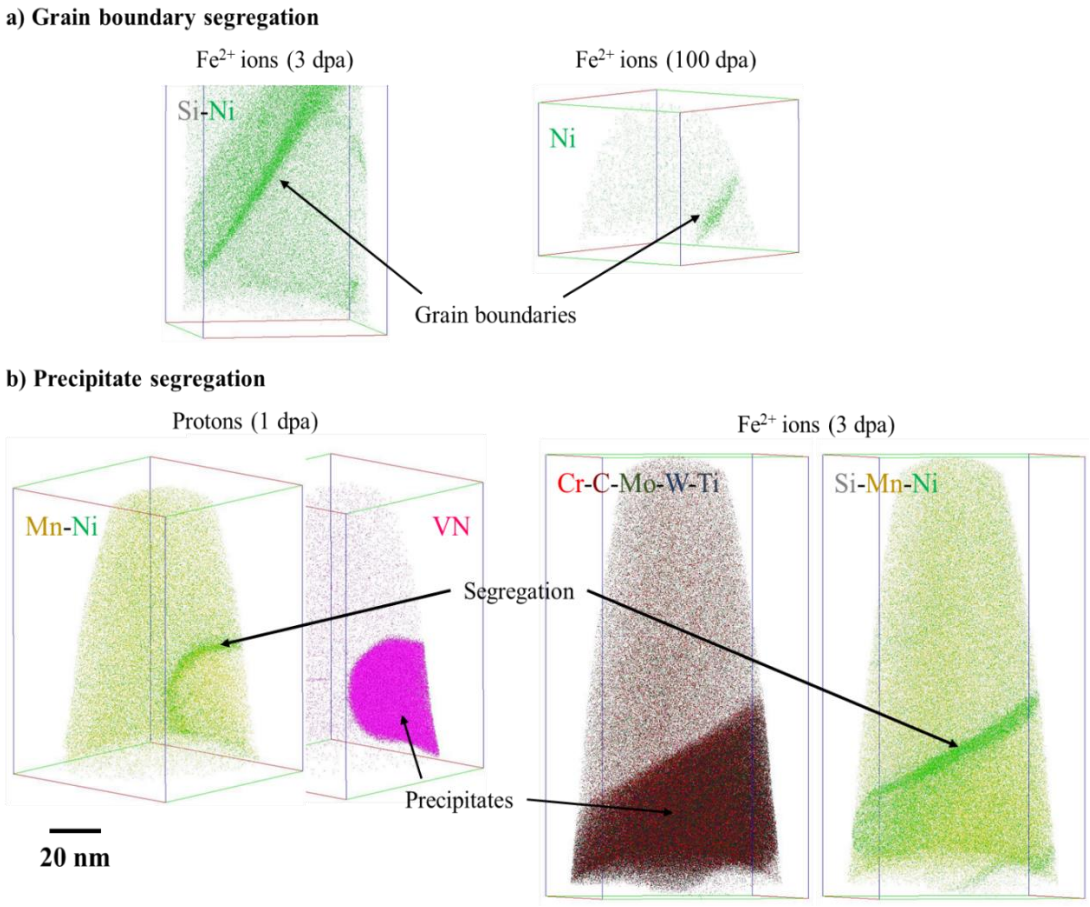

Figure 2.3. Examples of solute segregation found in irradiated specimens of F/M alloy HT9 at a) grain boundaries and b) VN and carbide precipitates. All LEAP data is from ref. [13].

By contrast, HCM12A contains ~6x more Cu than any of the other F/M alloys in this study, and contains the highest combined concentration of Si, Mn, and Ni. These differences appear to facilitate abundant nucleation sites for distinct clustering of Si-Mn-Ni-rich nanoclusters with Cu-rich clusters at adjacent locations following Fe^{2+} irradiation to 3 dpa (Table 1.4). However, these Cu-rich and Si-Mn-Ni-rich are no longer found after 100 dpa of Fe^{2+} irradiation (Table 1.4), despite an increased loss of these solutes from the matrix (Table 1.6 and Fig. 1.2). This apparent trend suggests that any irradiation-induced clusters are unstable at higher doses and that solutes are potentially migrating to more stable sinks such

as grain boundaries and precipitates. As with HT9, several examples of sink segregation are found within the LEAP samples from ref. [13] particularly following 100 dpa with Fe^{2+} ions (Fig. 1.7).

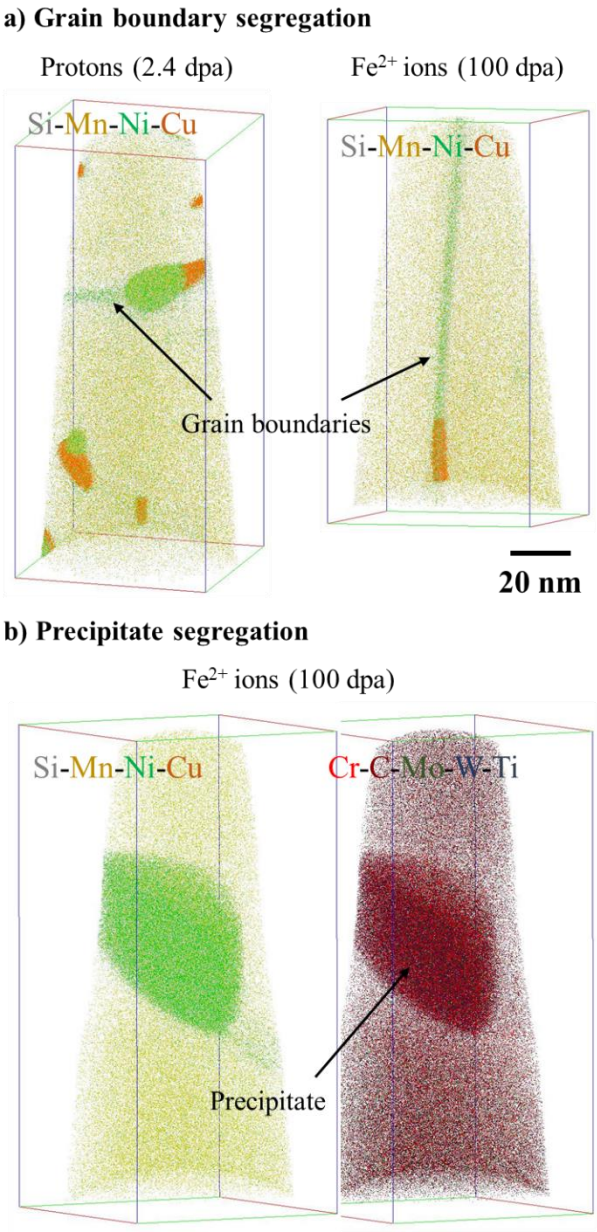

Figure 2.4. Examples of solute segregation found in irradiated specimens of F/M alloy HCM12A at a) grain boundaries and b) a carbide precipitate. All LEAP data is from ref. [13].

Alloy T91 contains only a marginal amount of Cu as well as the lowest combined amount of Si, Mn, and Ni solutes (Table 1.1) consistent with only a low volume fraction of Cu-rich and Si-Mn-Ni-rich clustering at 3 dpa. Furthermore, T91 has the lowest concentrations of C and N among the three alloys, likely correlating into fewer carbide and nitride precipitates (i.e. lower sink strength), which may explain why the reduction in matrix concentration of Si, Mn, Ni, and Cu is minimal. Once again, these clusters are no longer present at 100 dpa, even though solute concentrations in the matrix continue to decline after 100 dpa. As with HCM12A, this suggests that nanoclusters also unstable at higher dose as the solutes migrate to more stable sinks. As with the other F/M alloys, examples of distinct segregation to both grain boundary and precipitate sinks are found within the LEAP reconstructions from ref. [13,14], in (Fig. 1.8).

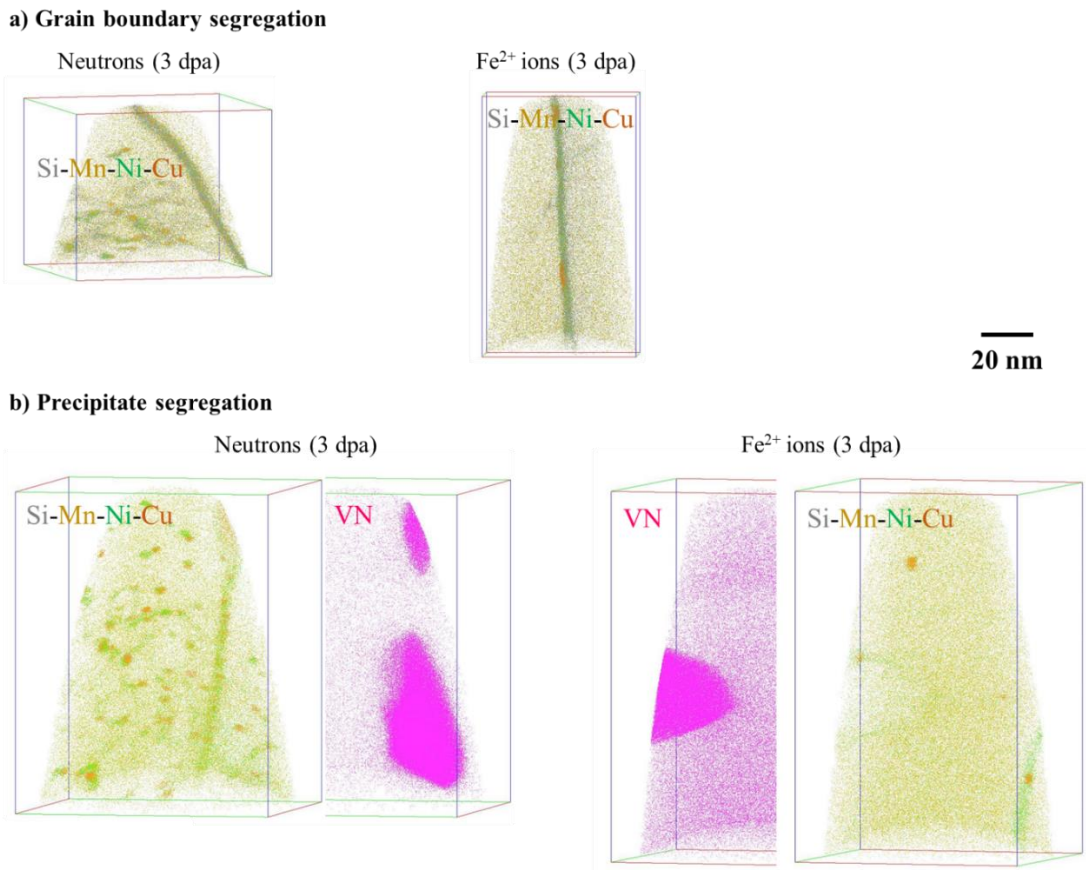

Figure 2.5. Examples of solute segregation found in irradiated specimens of F/M alloy T91 at a) grain boundaries and b) VN precipitates. All LEAP data is from ref. [14].

The irradiation-induced segregation of these solutes to various sinks within the microstructure is expected to influence the mechanical hardness and yield strength of each of these respective alloys. The formation of nanoclusters embedded within the matrix will have a hardening effect, potentially leading to embrittlement. Meanwhile, solutes dissolved within the matrix also have a strengthening effect, and when these solutes are removed from the matrix, a net softening of some amount is likely to occur. The following sections will explore the net influence of both solid solution strengthening and dispersed barrier hardening on the irradiation-induced evolution of the mechanical properties of each alloy.

Solid Solution Strengthening

To evaluate the effect of solutes migrating to and from the matrix on the mechanical properties of the materials, a solid solution strengthening model is developed to quantify the strengthening contribution of each species. As a byproduct of the cluster analysis routine in the IVAS software, quantification of the matrix composition surrounding the nanoclusters is readily available. From this data, the elemental composition of the surrounding matrix may be utilized in the solid solution strengthening model for a b.c.c. Fe matrix [39,40]:

$$\Delta\sigma_{ss,i} = K_i C_i \tag{2}$$

in which $\Delta\sigma_{ss,i}$ is the solid solution-induced change in yield strength, K_i is the strengthening coefficient of the solute element, and C_i is the matrix composition of the solute species. Through application of Eq. 2 for each solute element, the overall solid solution strengthening may be determined via the net sum of each individual species' contribution [46]. In many cases, several different values for the K_i coefficients may be found in archival literature and a summary of estimated values are retrieved from refs [39–41] and tabulated in Table 1.7, including the estimated values applied in this study. Given that each of the species of interest typically represent substitutional solutes, the strengthening coefficients for these solutes are similar and relatively low (15 – 50 MPa/at%) compared to their interstitial counterparts C, O, and N, which can have strengthening coefficients ranging 1000 – 1100 MPa/at% [39,42].

Table 2.7. Solid strengthening coefficients for solute elements (in MPa/at%), from refs. [39–41].

Solute	**Ref.** [39]	**Ref.** [40]	**Ref.** [41]	**Value used in this study, K_i**
Si	25.8	45	49-55	40
Mn	16.9	33	35-40	20
Ni	19.2	2.9	35-41	20
Cu	-	34	-	30

Using the strengthening coefficients from Table 1.7, and the matrix composition from Table 1.6, the overall solid solution strengthening is determined and summarized in Table 1.8. The estimated strengthening of the F/M alloys ranges ~28 – 46 MPa due to the four solutes of Si, Mn, Ni, and Cu within the matrix. Given that the overall measured irradiation-induced strengthening of these alloys range 51 – 206 MPa (Table 1.5) and the relatively large changes in matrix composition (Table 1.6) due to irradiation, it is possible that solid solution strengthening may have tangible influence on the mechanical properties.

Since we do not have APT data for the as-received specimens of these alloys, it is not clear if the solid solution strengthening has evolved dramatically as a result of irradiation with Fe^{2+} ions to 3 dpa. However, we can use the solid solution strengthening from Fe^{2+} irradiation to 3 dpa as a reference to estimate any change due to higher dose (100 dpa), or at lower dose rate (protons to 2.4 dpa). With this approach, irradiation with Fe^{2+} ions to 100 dpa is estimated to result in ~16 MPa reduction and ~2 MPa reduction in yield strength in HCM12A and T91, respectively, due to solute migration away from the matrix. Similarly, irradiation with protons to 2.4 dpa results in ~7 MPa reduction in yield strength in HCM12A. Although the magnitude of these values is relatively small, we continue to use them in our strengthening model for completeness. In the next sections, we combine the solid solution

strengthening and dispersed barrier hardening models to create a correlation between irradiation-induced changes in microstructure, microchemistry, and mechanical properties.

Table 2.8. Solid Solution Strengthening ($\Delta\sigma_{ss}$) of Si, Mn, Ni, and Cu solutes in irradiated specimens of HT9, HCM12A, and T91.

Solute, *i*	**HT9**		**HCM12A**						**T91**			
	Fe^{2+} ion-irradiated (3 dpa, 500 °C)		**Fe^{2+} ion-irradiated (3 dpa, 500 °C)**		**Fe^{2+} ion-irradiated (100 dpa, 500 °C)**		**Proton-irradiated (2.4 dpa, 500 °C)**		**Fe^{2+} ion-irradiated (3 dpa, 500 °C)**		**Fe^{2+} ion-irradiated (100 dpa, 500 °C)**	
	C_i (at%)	$\Delta\sigma_{ss,i}$ (MPa)	C_i (at%)	$\Delta\sigma_{ss,i}$ (MPa)	C_i (at%)	$\Delta\sigma_{ss,i}$ (MPa)	C_i (at%)	$\Delta\sigma_{ss,i}$ (MPa)	C_i (at%)	$\Delta\sigma_{ss,i}$ (MPa)	C_i (at%)	$\Delta\sigma_{ss,i}$ (MPa)
Si	0.26%	10.3	0.55%	22.0	0.30%	12.1	0.48%	19.2	0.59%	23.4	0.56%	22.3
Mn	0.65%	13.0	0.67%	13.5	0.69%	13.8	0.62%	12.4	0.44%	8.7	0.48%	9.6
Ni	0.15%	3.0	0.21%	4.1	0.04%	0.7	0.13%	2.6	0.17%	3.4	0.09%	1.9
Cu	0.06%	1.7	0.21%	6.3	0.12%	3.7	0.16%	4.8	0.14%	4.2	0.13%	3.9
Total $\Delta\sigma_{ss}$ (MPa)	-	28.0	-	45.9	-	30.4	-	39.0	-	39.8	-	37.6
$\Delta\sigma_{ss}^{irr}$ (MPa) above Fe^{2+}, 3 dpa	-	-	-	-	-	-16		-7	-	-	-	-2

Dispersed barrier hardening

Defect clusters including irradiation-induced features such as dislocation loops and voids, and solute nanoclusters within the microstructure act as barriers to dislocation motion and contribute to an irradiation-induced increase in the overall strength of the material. This increase in strength is often accompanied with reduced ductility and embrittlement [32,43–46], so it is necessary to have a clear understanding of the strengthening mechanisms. The most common approach for relating microstructure features to the yield strength is the simplified dispersed barrier hardening model [47]:

$$\Delta\sigma_{y,j} = \alpha_j M \mu b \sqrt{N_j d_j} \quad (3)$$

In this equation, M is the Taylor factor (3.06 for b.c.c. Fe-Cr alloys [29], μ is the shear modulus (82 GPa for F/M alloys [48]), b is the length of Burger's vector (0.248 nm [48]), N_j is the number density of feature type j, and d_j is the average diameter of feature j. The coefficient α_j represents the barrier strength of feature j and should range between 0 and 1. For each type of irradiation-induced feature characterized in the irradiated specimens, Eq. 3 may be applied and superimposed to estimate a net increase in yield strength from a network of features.

For the F/M alloys evaluated in this study, two separate types of nanoclusters are observed (Cu-rich and Si-Mn-Ni-rich) and characterized separately. However, these nanoclusters are observed to coexist predominantly at adjacent locations [13]. As a result, it is unlikely they will act as independent barriers to dislocation motion. To account for this, the respective average volumes for each nanocluster type are combined and a net effective diameter for the combined volumes is determined (as illustrated in Fig. 1.6). Next, to account for the fact that the Cu-rich nanoclusters are slightly more numerous in each of the irradiated specimens (Table 1.4), a weighted average of the combined effective diameter is determined using:

$$D_G^{comb} = \frac{D_G^{SiMnNiCu} N_{SiMnNi} + D_G^{Cu} N_{Cu}}{N_{comb}} \quad (4)$$

where the $D_G^{SiMnNiCu}$ is the effective diameter of the Si, Mn, Ni and Cu clusters resulting from a combined effective volume, N_{SiMnNi} is the number density of the Si-Mn-Ni-rich clusters, D_G^{Cu} is the average diameter of the Cu-rich clusters, and N_{comb} is the number density of the combined clusters and is equal the number density of the Cu-rich clusters. The

resulting combined effective diameters (Table 1.4) are estimated to be 10.66 nm and 7.44 nm for HCM12A irradiated with protons to 2.4 dpa and Fe^{2+} ions to 3 dpa, respectively. For T91 irradiated with Fe^{2+} ions to 3 dpa, the effective diameter is estimated to be 9.24 nm.

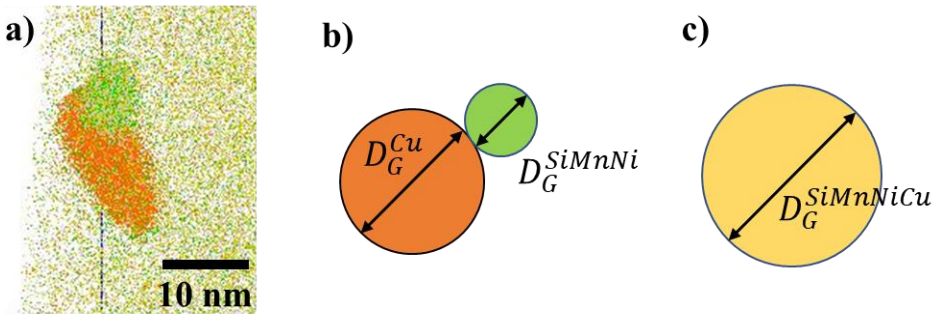

Figure 2.6. Illustration of the justification and approach to estimate a combined effective diameter ($D_G^{SiMnNiCu}$) of Si-Mn-Ni-Cu clusters showing: a) a typical pair of adjacent Cu-rich and Si-Mn-Ni-rich clusters, b) approximation of effective Guinier diameters for each solute cluster (not to scale), and c) the resulting effective combined Guinier diameter (not to scale) for use in the dispersed barrier hardening model.

Superposition of Solid Solution Strengthening and Dispersed Barrier Hardening

The methodology to evaluate the combined effects of the dispersed barrier hardening and solid solution strengthening models involves two inherent challenges. The first involves determining appropriate estimates for the respective strengthening coefficients of each dispersed feature in the microstructure (α_j), which sometimes cannot be directly fitted or solved via algebraic methods. The second challenge is to establish the appropriate method for superimposing the strengthening contribution of individual barriers to collectively correlate to measured strengthening values. Further complicating the analysis is that both of these challenges are interdependent, therefore often requiring a more deductive approach to estimating the strengthening coefficients.

For this study, two superposition methods are considered for combining the effects of multiple barriers to dislocation method: linear superposition and root-sum-square superposition [49]. Linear superposition is a straight summation of the contribution of each irradiation-induced feature and is expressed as:

$$\Delta\sigma_y^{lin} = \alpha_l M\mu b\sqrt{N_l d_l} + \alpha_{NC} M\mu b\sqrt{N_{NC} d_{NC}} + \alpha_V M\mu b\sqrt{N_V d_V} + \Delta\sigma_{ss}^{irr} \quad (5)$$

where $\Delta\sigma_{ss}$ is the net solid solution strengthening beyond the baseline strengthening (from Fe^{2+} irradiated to 3 dpa) given in the last row in Table 1.6.

Root-sum-square (rss) superposition is expressed as:

$$\Delta\sigma_y^{rss} = \sqrt{\Delta\sigma_{loops}^2 + \Delta\sigma_{nanoclusters}^2 + \Delta\sigma_{voids}^2} + \Delta\sigma_{ss}^{irr} \quad (6)$$

with the strengthening term for each dispersed barrier appearing under the radical, while the contribution of the solid solution strengthening is subsequently added to determine the net total. It is worth mentioning that a mixed approach for superposition was also developed in [50], but this approach requires prior knowledge of the α_j values for each barrier. As a result, the linear and root-sum-square superposition approaches in this study are considered to be lower and upper limits, respectively. In the following sections, a series of alternative analysis methods are applied to progressively deduce probable values for the strengthening coefficients of each dispersed barrier to correlate with measured strengthening (via nanoindentation) resulting from each irradiation on the three alloys.

Method 1: Analytical Approach with Incoherent Nanoclusters

The first approach involves estimation of the α values directly from analytical expressions, then evaluating both the linear and root-sum-square superposition methods to

predict irradiation-induced strengthening from the microstructure. For this initial approach, nanoclusters are taken as incoherent precipitates and are considered (along with loops and voids) as dispersed barriers contributing to strengthening. For this method, calculations are based on size- and density-dependent expressions developed by Tan and Busby [51], consistent with the notion that α factors may be dependent on the size and number density of the obstacles. The expressions for dislocations loops (thin plates), incoherent precipitates, and voids are defined as [51]:

$$\alpha_l = \frac{0.271A}{(1-\nu)^{1/2}\sqrt{Nd}(16-\pi tA)} ln\left(\frac{0.637d}{r_0}\right) \quad (7)$$

$$\alpha_{precip}^{incoh} = \frac{0.135}{(1-\nu)^{1/2}\left(1-0.816d\sqrt{Nd}\right)} ln\left(\frac{0.816d}{r_0}\right) \quad (8)$$

$$\alpha_v = \frac{0.383}{(1-\nu)^{1/2}\left(1-0.816d\sqrt{Nd}\right)} ln\left[\frac{0.247d}{r_0}\left(1-0.816d\sqrt{Nd}\right)\right] \quad (9)$$

where ν is Poisson's ratio (~0.33 [52–55]), $A = \sqrt{16\pi Nd} + 4Nd^2 - \pi^2 Ndt$ with *t* as the loop thickness (0.165 nm for {111} loops in b.c.c. Fe). For these equations, values for the dislocation core radii (r_0) are not well defined. Therefore, the approach outlined in [51] is applied by initially estimating $r_0 = b$ and fitting the initial estimated values for α to the function $\alpha = k_1 ln(k_2 d)$. Using the fitted values for k_2, estimations for r_0 are found to be ~0.81*b* and ~0.98*b* for loops and nanoclusters, respectively, while r_0 for voids remains 1.00*b* since fitting a curve to only one data point is not possible. Using these revised estimations for r_0 and Eq. 7-9, the α values are estimated for each respective feature in each irradiated specimen (Table 1.9).

The analytical values for α_l, α_{nc}, and α_v from this approach enable calculation of a predicted strengthening ($\Delta\sigma_y^{pred}$) for each of the irradiated microstructures using either linear superposition or root-sum-square superposition of the features. For these predictions, we have also subtractedany solid solution strengthening estimated in Table 1.8. Using this analytical approach, the predicted strengthening estimates are significantly higher than the measured values ($\Delta\sigma_y^{meas}$), particularly for specimens containing irradiation-induced nanoclusters. This result suggests that assuming the nanoclusters are incoherent may not be valid.

Table 2.9. Summary of values for strengthening coefficients (α) derived from several analysis methods. Predicted strengthening from each set of coefficients are determined using both linear and root-mean-square superposition and compared to measured strengthening values.

	Linear			Root-Sum-Square				Linear	RMS	Measured
	α_l	α_{nc}	α_v	α_l	α_{nc}	α_v	$\Delta\sigma_{ss}$	$\Delta\sigma_y^{pred}$	$\Delta\sigma_y^{pred}$	$\Delta\sigma_y^{meas}$
Method 1 - Analytical										
HT9, Fe^{2+} 3 dpa	0.48	-	-	0.48	-	-	0	115	115	86
HCM12A, p^+ 2.4 dpa	0.48	0.67	-	0.48	0.67	-	-7	761	613	186
HCM12A, Fe^{2+} 3 dpa	0.48	0.64	-	0.48	0.64	-	0	1246	1130	206
HCM12A, Fe^{2+} 100 dpa	0.55	-	0.84	0.55	-	0.84	-16	155	114	65
T91, Fe^{2+} 3 dpa	0.52	0.62	-	0.52	0.62	-	0	520	446	76
T91, Fe^{2+} 100 dpa	0.55	-	-	0.55	-	-	-2	156	156	51
Method 2 – Simple Fitting										
HT9, Fe^{2+} 3 dpa	0.35	-	-	0.35	-	-	0	86	86	86
HCM12A, p^+ 2.4 dpa	0.38	0.06	-	0.48	0.09	-	-7	186	186	186
HCM12A, Fe^{2+} 3 dpa	0.38	0.06	-	0.48	0.09	-	0	206	206	206
HCM12A, Fe^{2+} 100 dpa	0.38	-	-0.03	0.48	-	Neg.	-16	-	-	65
T91, Fe^{2+} 3 dpa	0.19	0.07	-	0.19	0.10	-	0	76	76	76
T91, Fe^{2+} 100 dpa	0.19	-	-	0.19	-	-	-2	51	51	51
Method 3 – Analytical/Fitted										
HT9, Fe^{2+} 3 dpa	0.22	-	-	0.22	-	-	0	52	52	86
HCM12A, p^+ 2.4 dpa	0.19	0.14	-	0.19	0.20	-	-7	185	186	186
HCM12A, Fe^{2+} 3 dpa	0.19	0.09	-	0.19	0.11	-	0	206	206	206
HCM12A, Fe^{2+} 100 dpa	0.25	-	0.41	0.25	-	0.94	-16	65	65	65
T91, Fe^{2+} 3 dpa	0.23	0.06	-	0.23	0.09	-	0	76	76	76
T91, Fe^{2+} 100 dpa	0.26	-	-	0.26	-	-	-2	73	73	51

Method 2: Simple Fitting

The next approach is to apply the strengthening Eqs. 5 and 6 for the microstructures of each irradiated specimen and solve for the respective α values of each feature that will enable the predicted strengthening ($\Delta\sigma_y^{pred}$) to match the measured strengthening ($\Delta\sigma_y^{meas}$). Fortunately, for each alloy we can write a series of strengthening equations for each irradiation condition and have a common number of equations and unknown variables. It is worth noting that this approach assumes that the α values are not dependent on size and

density, unlike the analytical approach in Method 1. Fitted values for each α are summarized in Table 1.9. The values determined for loops (α_l) are generally comparable to those found in Method 1, with the exception of the T91 specimen, which are ~%60 lower. On the other hand, values for nanoclusters (α_{nc}) are substantially lower than Method 1, suggesting that nanoclusters may be more coherent with the surrounding matrix. Finally, the fitted value for voids (α_v) is found to be negative using both the linear and root-sum-square superposition approaches, which does not represent a real solution for dispersed barrier hardening.

In the next section, we will look at a mixed approach leveraging analytical estimates and the fitting method to enable a real solution that more accurately predicts the measured strengthening.

Method 3: Mixed Analytical and Fitting

Two of the irradiated specimens in this study are observed to include only dislocation loops as irradiation-induced features: HT9 (Fe^{2+}, 3 dpa) and T91 (Fe^{2+}, 100 dpa) (Table 1.3). As a result, we can apply Eq. 3 for the dislocation loops and deduce estimated α_l values for these two specimens to find α_l in HT9 (Fe^{2+}, 3 dpa) is 0.35, while α_l in T91 (Fe^{2+}, 100 dpa) is 0.19. Next, applying these values in Eq. 7 enables determination of values for the dislocation core radius (r_0) to be 1.83b and 9.56b for the HT9 and T91 specimens, respectively. The value for r_0 in HT9 is consistent with the analytically deduced value for r_0 (~1.23b) found for a model ferritic Fe-9%Cr ODS alloy in a prior study [42], and previous studies have estimated the dislocation radius to typically range between b and 4b [3]. It is not clear why the r_0 for T91 is notably larger. Next, we initially apply the dislocation core radius from the HT9 specimen (r_0 = 0.45 nm) to calculate an analytical estimate for α_l for each of the other

irradiated microstructures. Using these values for α_l, the strengthening Eqs. 5 and 6 are then applied to solve for the remaining α values that will enable the predicted strengthening ($\Delta\sigma_y^{pred}$) to match measured strengthening ($\Delta\sigma_y^{meas}$). Unfortunately, this approach still results in a negative value for α_v in HCM12A (Fe^{2+}, 100 dpa), suggesting that the estimated strengthening coefficient for the dislocation loops is still too high.

To adjust this approach, both the analytically determined r_0 values for dislocation loops from HT9 (Fe^{2+}, 3 dpa) and T91 (Fe^{2+}, 100 dpa) are averaged to estimate r_0 = 1.41 nm (~5.69b). Once again, using this revised value for r_0, revised strengthening coefficients for dislocation loops are estimated for each irradiation condition, enabling fitting of the nanocluster and void strengthening coefficients for each irradiated alloy. The resulting values (Table 1.9) for α_l range 0.19 – 0.26, while α_{nc} values range 0.06 – 0.14 using linear superposition and range 0.09 – 0.20 using root-sum-square superstition, lower values suggesting that nanoclusters are more coherent with the matrix. Gupta et al. [56] note that α for loops and defect clusters for T91 proton irradiated at doses of 3, 7, and 9 dpa, and at temperatures of 400°C, 450°C, and 500°C to range from 0.2-0.3, which fall in line with results presented. Matijasevic et al. [57] found that α for loops of 0.5 in low dose (0.06 dpa) neutron irradiated Fe-9%Cr to be sufficient in determining the strengthening due to loops, but at higher doses it was visible that the loops were not the only defects to be responsible for the hardening of the alloy, and 0.5 is not an accurate representation. Shang et al. [58] noted that irradiation-induced nanoclusters can be reasonably estimated as relatively weak barriers and can be estimated with the DBH model with an $\alpha < 0.25$. The resulting value for α_v also ranges 0.41 – 0.94 depending on the superposition method, consistent with values found for voids (α_v = 0.60 – 0.65) in a prior hardening analysis in a model Fe-9%Cr ODS alloy [42].

Field et al. [59], reported similar strengthening coefficients for dislocation loops (0.17 - 0.33) and Cr-rich α' clusters in a model Fe-Cr-Al alloy. Bergner et al. [60] also studied a very similar series of Fe-Cr-based alloys with irradiation-induced Si-Mn-Ni-rich nanoclusters and report α values of 0.44 and 0.134 for dislocation loops and NiSiPCr-rich clusters, respectively, also consistent with the findings here.

Method 4: Analytical with Coherent Nanoclusters

For this final approach, we focus on evaluating the strengthening coefficients for the nanoclusters using an alternate analytical expression developed by Tan and Busby for spherical obstacles that are coherent with the matrix [51]:

$$\alpha_{nc}^{coh} = \frac{0.816\gamma_{nc}\boldsymbol{d}}{\mu b^2\left(1-0.816\boldsymbol{d}\sqrt{\boldsymbol{N}\boldsymbol{d}}\right)} + 1.7\left(\frac{\boldsymbol{d}}{b}\right)^{1.5}\varepsilon^{1.5} + 0.0054\left(\frac{\boldsymbol{d}}{b}\right)^{0.275}\left(\frac{\Delta\mu}{\mu}\right)^{1.5} \quad (10)$$

where μ is the shear modulus (82.0 GPa), b is equal to the burgers vector (0.248 nm), and d and N are the nanocluster average diameter and number density, respectively. This equation for α_{nc}^{coh} depends on three unknown parameters: interfacial energy, γ_{nc} (J/m^2); lattice parameter mismatch between the cluster and matrix, ε; and shear modulus mismatch between the cluster and the matrix, $\Delta\mu$ (GPa). If we allow each of these unknowns to vary for each irradiation-induced cluster morphology, there are far more unknown variables than there are strengthening equations, rendering the system unsolvable via algebra. As a result, the approach applied here is to evaluate the range of values for which $\Delta\mu$, ε, and γ_{nc} are valid (i.e. positive) to define a finite solution space for each set of variables using the α_{nc} values deduced in Method 3. The results of this exercise are illustrated in Fig. 1.7 for both linear superposition and root-sum-square superposition.

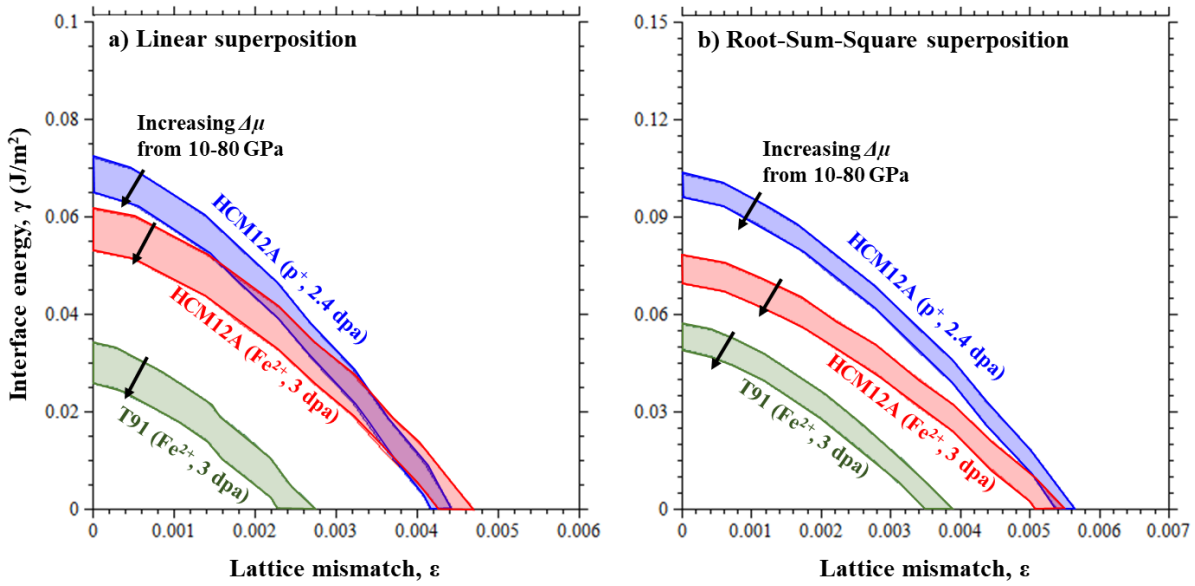

Figure 2.7. Solution space for γ_{nc}, ε, and $\Delta\mu$ from Eq. 10 used values of α_{nc} derived using Method 3 based on a) Linear superposition, and b) root-sum-square superposition of features in irradiated HCM12A and T91 alloys.

The nanoclusters in HCM12A following proton irradiation to 2.4 dpa appear to result in a slightly higher interfacial energy or lattice mismatch (or both) in comparison to the specimen irradiated Fe^{2+} ions to 3 dpa. This may be due to the coarser morphology of clusters following proton irradiation (Table 1.4), suggesting that larger clusters may trend toward a more incoherent structure as they grow. On the other hand, clusters in T91 appear to have a lower combination of interfacial energy and lattice mismatch. The reason for this is not clear but may be related to the relative Cu content in the alloys. Alloy T91 has much lower Cu composition, resulting in a much lower contribution to the effective diameter of the combined clusters. Since Cu is known to favor an f.c.c. structure upon precipitation, the reduced Cu content in the T91 clusters may conversely result in more coherent clusters.

Conclusion

In this study, three commercial ferritic-martensitic alloys were irradiated at 500°C to doses ranging 2.4 to 100 dpa with Fe^{2+} ions or protons. Nanoindentation measured the change in hardness as a result of each irradiation. Irradiation effects on solute migration is characterized using APT to complement a prior study using APT and TEM to irradiation-induced microstructure changes in the same specimens. The dispersed barrier hardening and solid solution strengthening models are combined to relate changes in microstructure and microchemistry to the measured changes in mechanical properties. Based on this analysis, the following conclusions are drawn:

1) Irradiation with Fe^{2+} ions at 500 °C results in Cu-rich and Si-Mn-Ni-rich nanoclusters after 3 dpa in HCM12A and T91, but these clusters are redissolved after 100 dpa, despite an increased loss of solutes in the matrix at the higher dose. The irradiation-induced clusters are not stable at higher doses as solutes appear to migrate to more stable sinks.
2) Dissolution of low-dose nanoclusters and segregation of solutes to other sinks at higher dose is expected to result in partial softening of the material, consistent with mechanical property measurements of both HCM12A and T91 irradiated with Fe^{2+} ions.
3) A model combining the dispersed barrier hardening and solid solution strengthening effects can reasonably predict the change in yield strength for 3 separate F/M alloys resulting from irradiation-induced evolution of microstructure and microchemistry.
4) Larger nanoclusters (and those with higher Cu content), such as those in HCM12A, tend to have higher strengthening coefficients. These clusters are found to likely have

a larger combination of interfacial energy and lattice mismatch with the matrix, suggesting they trend to toward less coherency with the surrounding matrix.

Chapter 3: Mechanical Property Evolution on Oxide Dispersion-Strengthened MA956 Alloy due to Friction Stir Welding, and Self-Ion Irradiation

Abstract

The objective of this study is to evaluate and numericize the effects of friction stir welding (FSW), and irradiation induced microstructure features in Oxide dispersion strengthened (ODS) alloy MA956 using the dispersed barrier hardening (DBH) model coupled with solid solution strengthening, and the grain size dependence (Hall-Petch) model. A large data set is presented including base material, and friction stir welding conditions, as well as irradiation levels of 1, and 25 dislocations per atom (dpa) at 400°C, 450°C, and 500°C. Nanoindentation was performed on all samples to determine the change in hardness due to friction stir welding, and a result of irradiation. Transmission electron microscopy (TEM) was used to determine microscopic level defects, and atom probe tomography (APT) was used to quantify the solutes in the matrix and the nanoclusters induced by irradiation. One comparison was made on the base material and stir zone, and with the use of the dispersed barrier hardening model, solid solution strengthening, and the grain size dependence (Hall-Petch) it was found that the solutes in the matrix, and the grain size dependence contribute to the overwhelming decrease in strengthening from the base material to the stir zone. Another comparison was made between 400°C 25 dpa stir zone, and 500°C 25 dpa stir zone, and the 400°C 25 dpa base material, and the 500°C 25 dpa base material to understand the effects of irradiation induced microstructure features in the stir zone, and base material. Several approaches were taken to understand that change in yield strength in these different conditions

Introduction

With rising global demand for low cost clean energy, nuclear fission and fusion systems will become increasing important energy sources for both economic and environmental reasons. A new generation of nuclear reactor (Gen IV) has been developed with a goal of high efficiency and low emissions. The Gen IV reactor will operate at a much higher efficiency than previous models but will cause a higher demand on the materials. These materials will need to withstand high temperatures (700°C) and adverse conditions (several hundred dpa). Small modular reactors have also gained popularity due to small capital cost and improved public perception. Qualities such as resistance to oxidation, resistance to swelling, and low levels of radioactivation will be critical for any material used in these systems. The material focused on in this study is an oxide dispersion-strengthened alloy, MA956.

Before ODS steels can be used in nuclear power plants, their ability to withstand high temperature, and high irradiation damage must be understood. It is well known that irradiation-induced microstructure features (dislocation loops, dispersoids, and nanoclusters) impede dislocation movement (i.e. increase in yield strength,) and will need to be quantified for each feature.

The dispersed barrier hardening model is the most commonly used approach for relating microstructure features to mechanical property changes. In this model the challenge is to estimate the strengthening coefficient for each obstacle.

The objective of this study is to evaluate the effects of friction stir welding and irradiation on the strengthening mechanisms of ODS alloy, MA956. The objective is achieved by developing a model that combines the dispersed barrier hardening with the solid

solution strengthening, and the grain size dependence models to accurately relate the microstructure features to the change in yield strength of the material. The study will accomplish this through evaluation of mechanical property changes resulting from FSW, and irradiation levels at 400°C, 450°C, and 500°C with 5 MeV Fe^{2+} ions with doses ranging 1 – 25 dpa and the combination of nanoindentation, TEM, and APT. Multiple approaches are taken for estimating strengthening coefficients for each feature, and applied using the linear superposition theorem.

Experiments

Materials, irradiations, and microscopy

The work in this study focuses on a fine-grained uncrystallized MA956 steel plate. The MA956 was canned and extruded at 1100°C and hot rolled in three passes at 1100°C over 4 hours with reheating to 1100°C 30 minutes before and after each rolling pass. The plate was then machined to a thickness of 4 mm. The chemical composition of MA956 is listed below in Table 2.1.

Following the manufacturing of the material, a single bead-on-plate on a sample of MA956 was conducted using the friction stir welding process by MegaStir technologies. A plunge force was maintained at 17.8 kN. The tool rotated at 500 rotations per minute (rpm) and the tool traversed at 25 mm per minute.

Specimens from the FSW process (stir zone), as well as base material were prepared by polishing using SiC paper up to a grit of P1200-P4000 followed by mechanically polishing up to 1 μm diamond polish, and finally polished using a vibratory polisher with a 0.02 μm colloidal silica solution to a mirror polish. The specimens were then irradiated at the Ion Beam Laboratory at Sandia National Laboratory, with a 6 MV Pelletron accelerator with

5 MeV Fe^{2+} ions with a raster scanned beam. Samples were irradiated at 1 and 25 dpa at 400°C, 450°C, and 500°C. Dose was calculated and verified at a depth of 600 nm using the Quick Kinchin Pease Mode in SRIM with a displacement of 40 eV. Does rates vary from 0.44-2.3 x 10^{-4} dpa/s.

Table 3.1. Summary of irradiation conditions evaluated in this study.

Alloy		**5 MeV Fe^{2+} ions (0.44-2.3 x 10^{-4} dpa/s)**		
	As-received	**400°C**	**450°C**	**500°C**
MA956	Base Metal	1, 25 dpa	1, 25 dpa	1, 25 dpa
	Stir Zone	1, 25 dpa	1, 25 dpa	1, 25 dpa

Transmission electron microscopy (TEM) was used to analyze the specimens and evaluate microscopic microstructure evolution invoked by irradiation. Focused ion beam (FIB) techniques were used for all irradiation conditions as well as as-received conditions.

Atom probe tomography was conducted to analyze the specimens and evaluate nanostructure features. APT complements TEM in analyzing and evaluating nanoclustering of solutes, and the matrix solute chemistry following each irradiation condition of the sample.

Table 3.2. Composition of MA956 heat used in this research [61] determined by inductively coupled plasma mass spectrometry and LECO analysis.

Alloy	Fe	Cr	Al	Y2O3	Ti	Mn	Si	Ni	C	Mo	S	P
MA956 (wt %)	Bal	19.93	4.75	0.51	0.39	0.09	0.08	0.04	0.023	0.02	0.008	0.006

Nanoindentation

Nanoindentation was conducted on each specimen to understand and evaluate the hardness changes between the base material irradiated conditions to the stir zone irradiated conditions. A quasi-static stiffness measurement technique was used to retrieve hardness and modulus results. In quasi-static testing, the indenter head penetrates to a desired depth, holds then measures the elastic stiffness on retraction. This gives only discrete points at which properties are known, but avoids any issues arising from other methods. Nanoindentation was conducted using a KLA-Tencor G200 nano-indenter. A surface detection threshold stiffness of 200 N/m was used; this parameter is used to identify the sample surface when the tip makes contact. If this parameter is set too low, signal noise will cause contact in the surface prematurely, and if set too high it will indent into the surface before the data collection process is started. In both cases, this displacement, hardness, and modulus will be misreported, and data will be skewed. Tip calibration was used on a sample of fused silica with known calibration variables. A 2^{nd}-order polynomial function was fitted, and an analysis was done in NanoSuite, a software using the Oliver-Phar Method. [20]

Measurements of each sample were conducted at the University of Idaho in Moscow, ID. using a displacement-controlled method. A Berkovich diamond tip indenter was used. As-received base metal and stir zone samples were previously mounted in an epoxy-resin puck, and irradiated samples were mounted onto glass slides with mount wax, and then adhered to an aluminum puck. The indentations were made parallel to the irradiated surface

and indented in 20-25 locations. The indents were spaced 25-60 μm apart to avoid plastic zone interference, since the plastic zone is expected to be ~4-5 times deeper than the indent itself [21–26]. The tip was loaded and unloaded at 10 depths per indent site. Each indent load cycle included a 15-second load time with a 10-second hold time at maximum load, and then unloaded to 90% of the previous load. For each indent location, the average depth was determined at each 10 depths, and the average hardness and modulus were calculated with a standard deviation of the mean for both values. A modulus was calculated at each depth as well to ensure overall calibration was correct.

Results

Transmission electron microscopy

The microstructure of the alloy was characterized in research done by Dr. Elizabeth Getto at the United States Naval Academy. A summary of the microstructure is present in the table below. Average characteristics of dispersoids, and dislocations per material condition are noted in Table 2.3. Not noted in the table, but a very important microstructure feature to assess is the change in average grain size change due to friction stir welding. The average grain size of base material is 0.89 μm which increases in size to an average of 12.5 μm in the stir zone [62].

Table 2.3. Summary of microstructure measurements using TEM. Errors are reported as the standard deviation.

			Dispersoids			Dislocations					
Temperature (°C)	Dose (dpa)		Number of Precipitates	Precipitate diameter (nm)	Precipitate Density (10^{20} m^{-3})	Number of Loops	Loop Diameter (nm)	Loop Number Density (10^{20} m^{-3})	Loop Line Length (10^{14} m^{-2})	Network Line Length (10^{14} m^{-2})	Total Line Length (10^{14} m^{-2})
As received	N/A	BM	263	10.6±1.0	8.96±0.9	N/A	N/A	N/A	N/A	0.614±0.1	0.614±0.1
		SZ-H	103	19.7±1.0	2.01±0.2					0.675±0.1	0.675±0.1
400	1	BM	536	8.1±1.0	12.3±1.2	70	9.5±1.0	35.2±7.0	2.1±0.5	1.6±0.4	3.7±0.9
		SZ-H	275	19.5±1.0	3.37±0.4	70	12.6±1.0	18.0±4.0	1.4±0.3	1.0±0.2	2.5±0.7
	25	BM	446	10.8±1.0	4.79±0.5	14	28.0±1.0	6.0±1.2	1.0±0.2	1.1±0.2	2.1±0.5
		SZ-H	67	18.0±1.0	2.25±0.2	44	15.8±1.0	13.0±2.6	1.3±0.2	1.1±0.2	2.4±0.7
450	1*	BM	393	10.4±1.0	10.8±1.0	17	20.2±1.0	6.2±1.2	0.8±0.2	1.2±0.3	2.0±0.5
		SZ-H	68	21.4±1.0	3.43±0.3	32	19.7±1.0	5.8±1.2	0.7±0.1	1.4±0.4	2.1±0.5
	25*	BM	164	11.5±1.0	5.13±0.5	40	20.6±1.0	6.3±1.2	0.8±0.2	0.7±0.2	1.5±0.4
		SZ-H	149	21.4±1.0	2.06±0.2	35	15.6±1.0	10.3±2.0	1.0±0.2	0.6±0.2	1.6±0.4
500	1	BM	662	10.1±1.0	10.1±1.0	21	20.9±1.0	1.9±0.4	0.3±0.1	0.9±0.2	1.2±0.3
		SZ-H	103	24.5±1.0	1.64±0.2	21	22.1±1.0	2.7±0.6	0.4±0.1	0.9±0.2	1.3±0.3
	25	BM	271	17.0±1.0	3.06±0.3	19	37.0±1.0	4.9±1.0	1.2±0.3	1.4±0.4	2.5±0.7
		SZ-H	187	22.0±1.0	2.10±0.2	20	50. ±1.06	0.9±0.2	1.1±0.2	0.6±0.2	1.7±0.5

Atom probe tomography

To achieve an objective characterization of irradiation induced solute clustering, APT was used to quantify the average size and number density of nanoclusters as well as any changes to the solute matrix composition. A summary of the APT is provide in tables 2.4 and 2.5.

Table 2.4. Summary of nanocluster characterization and matrix composition measurements of the base material using APT. Errors are reported as standard deviation of the mean.

Feature	MA956			
	BM			
	As Received	(25 dpa, 400 °C)	(25 dpa, 450 °C)	(25 dpa, 500 °C)
Analysis Volume (nm^3)	12,025,175	1,617,300	1,102,445	5,217,925
Oxide Nanoclusters				
# of nanoclusters measured	473	165	119	616
Average Diameter (nm) D_G^{NC}	7.42 ± 0.10	5.44 ± 0.16	5.57 ± 0.15	6.94 ± 0.07
Number Density (x 1021 m^{-3}) N_{nc}^{NC}	40	100	108	114
Volume fraction	0.93%	1.26%	0.64%	1.50%
Y:Ti	5.53 ± 0.13	3.59 ± 0.13	7.07 ± 0.62	7.97 ± 0.20
(Y+Ti):O	1.24 ± 0.01	1.09 ± 0.02	1.28 ± 0.02	1.21 ± 0.01
Al:O	3.14 ± 0.04	2.09 ± 0.04	2.56 ± 0.06	3.68 ± 0.04
Matrix Composition (at%)				
Y	0.05	0.12	0.08	0.09
Ti	0.07	0.12	0.08	0.07
O	0.13	0.26	0.26	0.22
Y+Ti+O	0.25	0.5	0.42	0.37

Table 2.5. Summary of nanocluster characterization and matrix composition measurements of the stir zone using APT. Errors are reported as standard deviation of the mean.

Feature	MA956			
	SZ			
	As Received	(25 dpa, 400 °C)	(25 dpa, 450 °C)	(25 dpa, 500 °C)
Analysis Volume (nm^3)	1,530,107	1,800,578	3,781,196	1,200,447
Matrix Composition (at%)				
Y	-	-	-	-
Ti	0.05	0.04	0.10	0.03
O	0.07	0.09	0.11	0.09
Y+Ti+O	0.12	0.12	0.21	0.11

Nanoindentation

Nanoindentation for the base metal, stir zone, and irradiated specimens was conducted for each condition. Indentation on all conditions are illustrated as a function of indentation depth vs. hardness. A comparison of the base material conditions vs. the stir zone

conditions, and irradiation conditions of 400°C and 500°C were made. The materials were indented at 100 – 1000 nm with a main comparison region of 500-650 nm to ensure that the nanoindentation was sampling the damaged area induced by irradiation. Using the comparison region, an overall hardness and standard deviation of the mean is calculated to establish an estimated mean hardness for each condition.

For the MA956 alloy, the nanohardness is estimated to be 4.35 ± 0.05 GPa, and 3.53 ± 0.04 GPa for the as-received base metal, and the as-received stir zone respectively. With a reasonably large quantity of indents, and a very narrow range for the standard deviation, this indicates that the as-received base material specimen is harder than the stir zone as-received specimen, which is shown in Figure 2.1. For the irradiation conditions of the base material at 400°C, 25 dpa vs. base material 500°C, 25 dpa, the nanohardness is estimated to be 4.22 ± 0.05, and 4.19 ± 0.04 respectively, indicating a decrease in hardness in the 500°C 25 dpa sample. The next comparison that was made was the 400°C 25 dpa stir zone vs. 500°C 25 dpa stir zone. Very similar to the previous comparison, the nanohardness values are estimated to be 3.33 ± 0.11 and 3.10 ± 0.04 respectively. Friction stir welding causes a decrease in hardness across all irradiation conditions. Within the different irradiation temperature conditions, a comparison was made between the irradiation damage doses. In the 400°C irradiation temperature there was a decrease in hardness in the base material of 0.14 GPa from the 1 dpa to the 25 dpa, and a decrease in hardness from the 1 dpa to the 25 dpa of 0.28 GPa in the stir zone. Similarly, in the 500°C there was a decrease in hardness in the base material of 0.17 GPa from the 1 dpa to the 25 dpa and decrease in hardness from the 1 dpa to the 25 dpa of 0.23 GPa in the stir zone.

Figure 3.1. Nanoindentation hardness measurements via indentation parallel to the irradiation beam at various depths in irradiated MA956. a) Base material vs. Stir zone b) 400°C 25 dpa stir zone vs. 500°C 25 dpa stir zone c) 400°C 25 dpa base material vs. 500°C 25 dpa base material d.) Summary of nanohardness measurements.

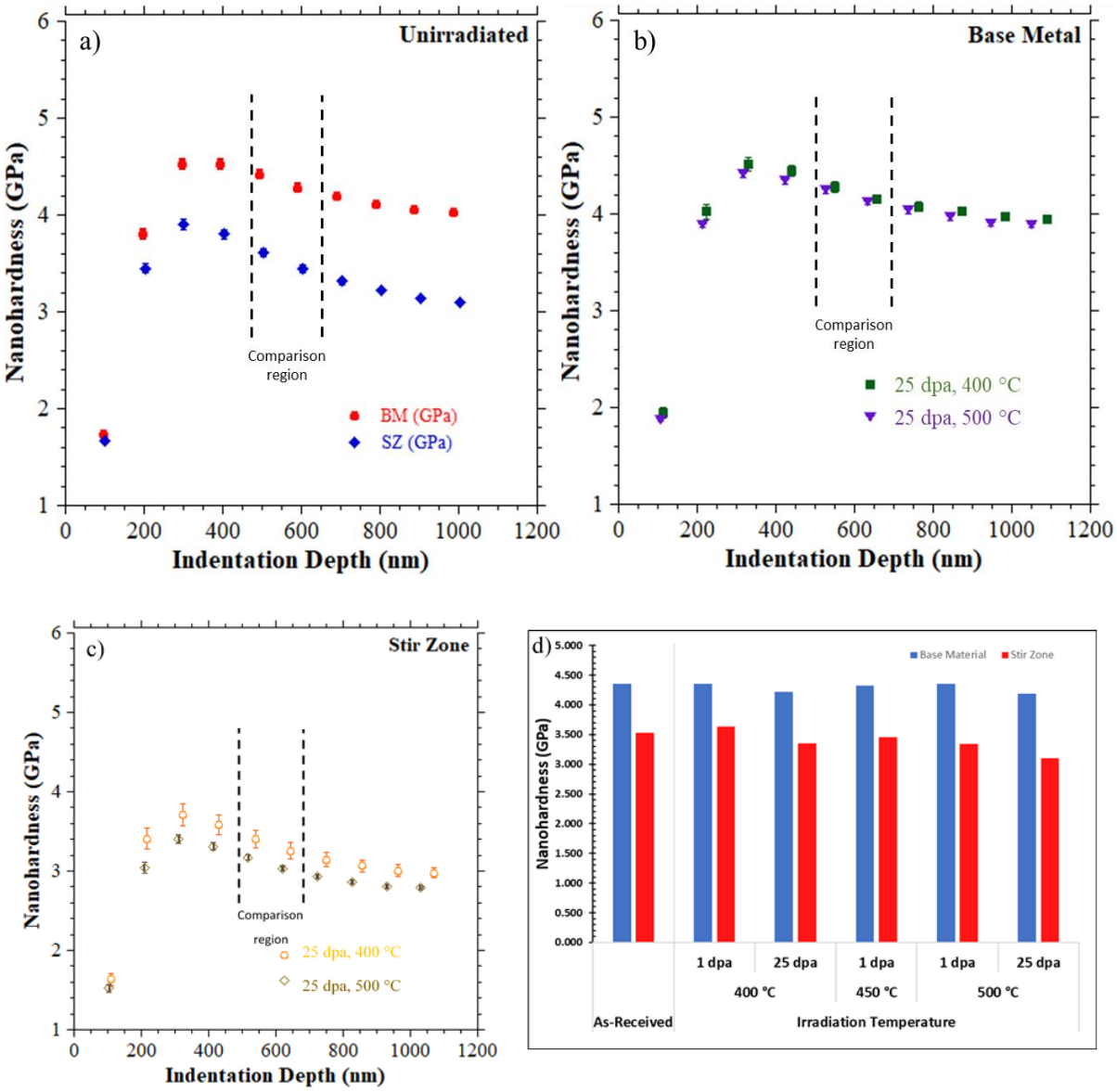

Nanohardness measurements are particularly helpful in estimating the decrease in strength as a result of friction stir welding. We can use the imperial relationship [29]:

$$\Delta\sigma_y = 3.06\Delta H_v \quad (1)$$

with $\Delta\sigma_y$ representing the increase in yield strength (in MPa) due to irradiation and ΔH_v as the measured increase in Vickers hardness (in kg/mm^2). In this case, we use the relationship developed by Fischer-Cripps to convert Berkovich hardness (in GPa) into Vickers hardness (in kg/mm^2) via $H_V = 94.495 H_{Berk}$ [30]. Following this approach, the change in yield strength for the base material, and stir zone is estimated to be -257 MPa. In the 400°C 25 dpa there is a change of -270 MPa, and in the 500°C 25 dpa there is a change of -338 MPa. A complete summarization of the estimated nanohardness and decreases in yield strength for the different conditions is provided in Table 2.3.

Table 3.3. Summary of nanohardness measurements and estimated decrease in yield strength.

Properties	As-received		400°C				450°C		500°C			
	Base Material	**Stir Zone**	**Base Material (1 dpa)**	**Stir Zone (1 dpa)**	**Base Material (25 dpa)**	**Stir Zone (25 dpa)**	**Base Material (1 dpa)**	**Stir Zone (1 dpa)**	**Base Material (1 dpa)**	**Stir Zone (1 dpa)**	**Base Material (25 dpa)**	**Stir Zone (25 dpa)**
Nanohardness, H_{Berk} (GPa)	4.354 ± 0.047	3.529 ± 0.038	4.359 ± 0.054	3.630 ± 0.049	4.215 ± 0.048	3.327 ± 0.105	4.322 ± 0.071	3.457 ± 0.035	4.352 ± 0.029	3.337 ± 0.081	4.187 ± 0.037	3.103 ± 0.035
Nanohardness, ΔH_{Berk}	-	-0.825	-	-0.729	-	-0.888	-	-0.865	-	-1.015	-	-1.085
Yield strength, $\Delta\sigma_y$ (MPa)	-	-257	-	-227	-	-277	-	-270	-	-316	-	-338

Discussion

Dispersed barrier hardening

Irradiation-induced defects such as dislocation loops, and nanoclusters act as barriers to dislocation motion and contribute to the overall strengthening of the material. While there is an irradiation induce strength increase, it is important to also note the grain development induced by friction stir welding. It is important and necessary to quantify and have a clear understanding of how each of these defects or features contribute to the effect of the yield strength of the material. The most common approach for relating these features to the yield strength is the simplified disperse barrier hardening model [47]:

$$\Delta\sigma_{y,j} = \alpha_j M \mu b \sqrt{N_j d_j} \tag{2}$$

In this equation, M is the Taylor factor (3.06 for b.c.c. Fe-Cr alloys [29], μ is the shear modulus (82 GPa for F/M alloys [48]), b is the Burger's vector (0.248 nm [48]), N_j is the number density of feature type j, and d_j is the average diameter of feature j. The coefficient α_j represents the barrier strength of feature j and should range between 0 and 1. For each type of irradiation-induced feature characterized in the irradiated specimens, Eq. 2 may be applied and superimposed to estimate an net increase in yield strength from a network of features.

A previous study done by Baker et al. [62] experimentally determined the overall strengthening caused by grain growth using the same set of friction stir welded specimens. Their experiments found that an average of 130 MPa can be attributed to the overall strengthening of a material from the stir zone to the base material. Found in figure 2.2 is a

graph relating grain size to the strength of the material using different methods of friction stir welding on MA956 completed by Baker et al. [62].

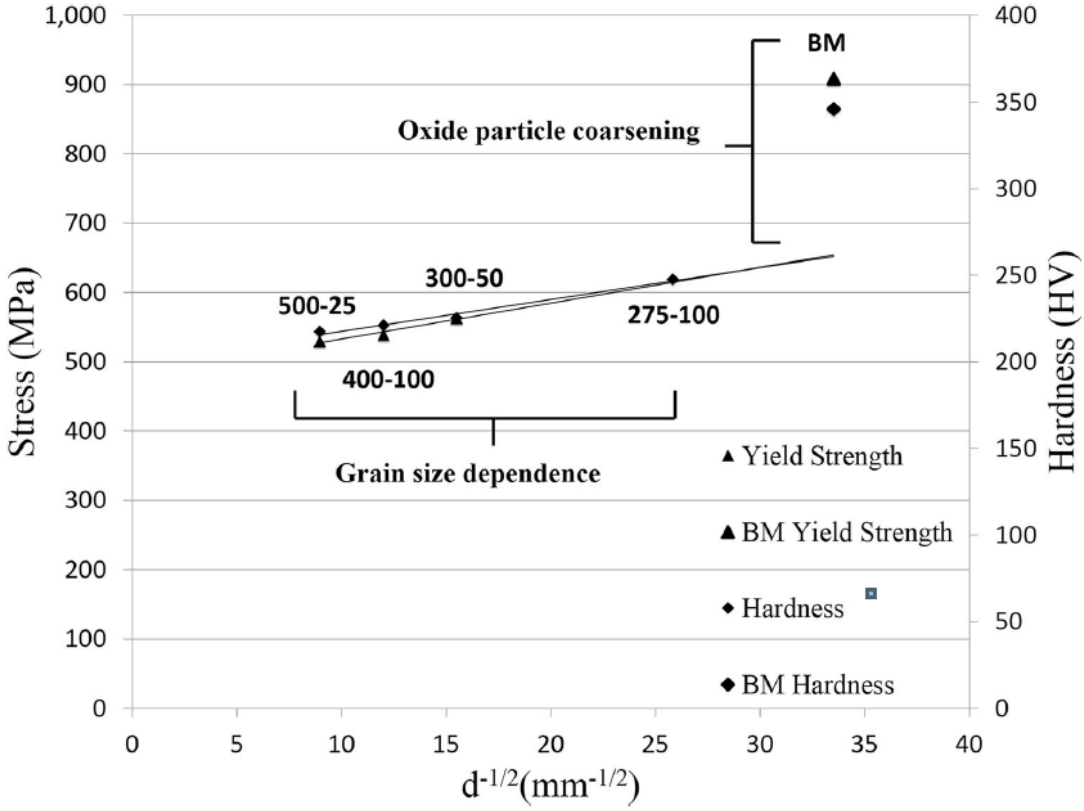

Figure 3.2. Comprehensive experimentally determined Hall-Petch plot of MA956, showing grain size dependence of yield strength from variations of friction stir welding parameters. 500 RPM – 25 MMPM were used in the case of this study [62].

Solid Solution Strengthening

To evaluate the effect of solutes migrating to and from the matrix, a solid solution strengthening model is developed to quantify the strengthening contribution of each species. As a byproduct of the cluster analysis routine in the IVAS software, quantification of the matrix composition surrounding the nanoclusters is readily available. From this data, the elemental composition of the surrounding matrix may be utilized in the solid solution strengthening model for a b.c.c. Fe matrix [39,40]:

$$\Delta\sigma_{ss,i} = K_i C_i \quad (3)$$

in which $\Delta\sigma_{ss,i}$ is the solid solution-induced change in yield strength, K_i is the strengthening coefficient of the solute element, and C_i is the matrix composition of the solute species. Through application of Eq. 2 for each solute element, the overall solid solution strengthening may be determined via the net sum of each individual species' contribution [46]. Using the equation above, the overall solid solution strengthening is determined, and summarized in Table 2.4. The base metal of each irradiation condition is used to determine the change in yield strength due to the matrix solid solution.

Table 3.4. Solid Solution Strengthening ($\Delta\sigma_{ss}$) of Y, O, and Ti solution in friction stir welded MA956 using base material of each irradiation condition as a baseline.

Solute, *i*	**MA956**											
	Base Metal As Received		**Stir Zone As-Received**		**Base Metal 25 dpa, 400°C**		**Stir Zone 25 dpa, 400°C**		**Base Metal 25 dpa, 500°C**		**Stir Zone 25 dpa, 500°C**	
	C_i (at%)	$\Delta\sigma_{ss,i}$ (MPa)	C_i (at%)	$\Delta\sigma_{ss,i}$ (MPa)	C_i (at%)	$\Delta\sigma_{ss,i}$ (MPa)	C_i (at%)	$\Delta\sigma_{ss,i}$ (MPa)	C_i (at%)	$\Delta\sigma_{ss,i}$ (MPa)	C_i (at%)	$\Delta\sigma_{ss,i}$ (MPa)
Y	0.05%	1.0	0.003%	0.1	0.12%	2.5	0.00%	0	0.09%	1.7	0.00%	0
O	0.13%	145.2	0.07%	77.0	0.26%	281.6	0.09%	94.6	0.22%	240.9	0.09%	94.6
Ti	0.07%	1.4	0.05%	1.0	0.12%	1.6	0.04%	0.7	0.07%	1.3	0.03%	0.6
Total $\Delta\sigma_{ss}$ (MPa)	-	147.6	-	78.1	-	286.5	-	95.3	-	244	-	95.2
$\Delta\sigma_{ss}^{irr}$ (MPa)	-	-	-	-69.5	-	-	-	-191.2	-	-	-	-148.8

Superposition of Solid Solution Strengthening, Hall-Petch and Dispersed Barrier Hardening

The methodology to evaluate the combined effects of the dispersed barrier hardening, solid solution strengthening, and the grain size dependence (Hall-Petch) models involves

many challenges. The first involves determining the appropriate estimates for the respective strengthening coefficients of each feature in the microstructure. The model cannot be simply solved for via algebraic methods, and must be solved using correlations, and limits known by previous implementations.

For this study, a linear superposition method is considered for combining the effects of multiple barriers to dislocation motion. Linear superposition is a straight summation of the contribution of each irradiation induced feature, and FSW induced changes. It can be expressed as:

$$\Delta\sigma_y^{lin} = \alpha_l M\mu b\sqrt{N_l d_l} + \alpha_{NC} M\mu b\sqrt{N_{NC} d_{NC}} + \alpha_V M\mu b\sqrt{N_V d_V} + \Delta\sigma_{ss}^{irr} + \Delta\sigma_{HP}^{FSW} \quad (4)$$

where $\Delta\sigma_{ss}$ is the net solid solution strengthening beyond the baseline strengthening, and $\Delta\sigma_{HP}$ is the net strengthening induced by the change in grain size from FSW.

Base Metal/Stir Zone

The first comparison that was evaluated was the relationship of the base metal vs. the stir zone across all irradiation conditions. This comparison was made to understand, and determine the overall strengthening decrease due to friction stir welding. Following nanoindentation it was clear that the stir zone is much softer than the base material. An average difference of -0.878 GPa was measured resulting in a change of -273.8 MPa in yield strength. Once this softening was measured, the dispersed barrier hardening model was paired with the solid solution strengthening, and the Hall-Petch model to quantity, and determine what microstructure features caused a decrease in yield strength. Using Eq. 4, the solid solution data in Table 2.4, and the dependence of grain size on yield strength (Figure 2.2), the following conclusions were made. In each irradiation condition it was clear that the

majority of the strengthening decrease was caused by the increase in grain size from base metal to stir zone, as well as the decrease in strengthening determined by the solid solution model. With the addition of both changes in yield strength, there leaves little to no room in determining the addition to strengthening from irradiation induced microstructure features (dislocation loops, dispersoids, and nanoclusters.) If these features were to be numericized it would indicate an overestimation of the change in yield strength. Grain size dependence and solid solution strengthening are the leading cause in the change in yield strength, and irradiation induced microstructure features must be negligible in a comparison of the base material to the stir zone. Tabulated below are the estimations of change in yield strength with the grain size dependence, and the solid solution strengthening.

Table 3.5. Estimation of the change in yield strength from base metal to stir zone. Predicted strengthening **(**$\Delta\sigma_y^{pred}$**)** from the grain size dependence, and the solid solution strengthening are determined by using the linear superposition theorem and compared to measured strengthening **(**$\Delta\sigma_y^{Meas}$**)** values.

	MA956		
	Base Metal-Stir Zone As Received	**Base Metal-Stir Zone 25 dpa, 400°C**	**Base Metal-Stir Zone 25 dpa, 500°C**
Grain Size Dependence ($\Delta\sigma_{HP}$)	-130	-130	-130
S.S.S ($\Delta\sigma_{ss}$)	-69.5	-192.2	-148.8
$\boldsymbol{\Delta\sigma_y^{pred}}$	-199.5	-322.2	-278.8
$\boldsymbol{\Delta\sigma_y^{Meas}}$	-257	-270	-338

400°C-500°C Stir Zone Comparison

The next comparison that was made was a comparison between the 400°C 25 dpa stir zone vs. the 500°C 25 dpa stir zone. This method is used to understanding the effects of temperature dependence in the irradiation process and quantify the strengthening factors in irradiated materials that have been friction stir welded. The dispersed barrier hardening model was coupled with the solid solution strengthening model to determine how each microstructure feature was adding to the overall change in strengthening. Within the stir zone, only dislocation loops and dispersoids were present. Calculations were made based on size and density dependent equations developed by Tan and Busby [51], which assumes α values for each feature, resulting in the contribution to the change in yield strength from each irradiation temperature. The α for dislocation loops, and dispersoids are defined as [51]:

$$\alpha_l = \frac{0.271A}{(1-\nu)^{1/2}\sqrt{Nd}(16-\pi tA)} ln\left(\frac{0.637d}{r_0}\right) \quad (5)$$

$$\alpha_{precip}^{incoh} = \frac{0.135}{(1-\nu)^{1/2}\left(1-0.816d\sqrt{Nd}\right)} ln\left(\frac{0.816d}{r_0}\right) \quad (6)$$

where ν is Poisson's ratio (~0.33 [52–55]), $A = \sqrt{16\pi Nd} + 4Nd^2 - \pi^2 Ndt$ with *t* as the loop thickness (0.165 nm for {111} loops in b.c.c. Fe). For these equations, values for the dislocation core radii (r_0) are not well defined. Therefore, the approach outlined in [51] is applied by initially estimating $r_0 = b$ and fitting the initial estimated values for α to the function $\alpha = k_1 ln(k_2 d)$. Using the fitted values for k_2, estimations for r_0 are found to be 0.326, and 0.377 for dispersoids, and loops, respectively.

The analytical values for α_l, and α_{disp} from this approach allow for a calculation of the change in predicted strengthening ($\Delta\sigma_y^{pred}$) for each of the different irradiation temperature using the linear superposition theorem. Results from this method are tabulated below in Table 2.6.

Table 3.6. Summary of values for strengthening coefficients of loops (α_l), and dispersoids (α_{disp}) at temperatures of 400°C, and 500°C, and change in the solid solution strengthening. Predicted overall change in strengthening from irradiation temperatures using the linear superposition theorem compared to the measured strengthening values.

	MA956	
	400°C 25 dpa Stir Zone	**500°C 25 dpa Stir Zone**
α_l	0.501	0.565
α_{disp}	0.647	0.687
S.S.S ($\Delta\sigma_{ss}$)	-0.1	
$\Delta\boldsymbol{\sigma_y^{pred}}$	-55.9	
$\Delta\boldsymbol{\sigma_y^{Meas}}$	-77	

400°C-500°C Base Metal Comparison

The final approach that was taken, was a comparison of the base material at 400°C, 25 dpa vs. 500°C, 25 dpa. Within the base metal at these irradiation conditions there are many microstructure features that are present, these include dislocation loops, dispersoids, and nanoclusters. This method will give a better understanding of the effects of irradiation temperature in the base material. Within this caparison, two different approaches are taken to

determine the strengthening coefficients of the microstructure features. Unlike the stir zone, nanoclusters are present in the base material which makes determining each coefficient a little more challenging. In approach I below, the nanoclusters are assumed to be incoherent, and in approach 2 the nanoclusters are assumed to be incoherent.

Approach I – Incoherent Nanoclusters

In this approach, a similar method to the stir zone comparison is conducted. The analytical Eq. 5 and 6 provided by Tan and Busby [51] are used to determine each strengthening coefficient at 400°C and 500°C. These features are considered to act incoherently in the matrix and can be quantified as such. While these equations have been proven to accurately determine dislocation loops, and dispersoids their use when determining the strengthening coefficients of nanoclusters have shown to give an overestimation of applied strengthening of the material. In the table below, the strengthening coefficients of the microstructure features has been tabulated with the overall predicted change in yield strength, and the measured yield strength. The predicted yield strength is extremely overestimated, and in the following approach a method to best estimate the yield strength will be determined.

Table 3.7 Summary of values for strengthening coefficients of loops (α_l), dispersoids (α_{disp}), and nanoclusters (α_{nc}) at temperatures of 400°C, and 500°C, and change in the solid solution strengthening. Predicted overall change in strengthening from irradiation temperatures using the linear superposition theorem compared to the measured strengthening values.

	MA956	
	400°C 25 dpa Base Material	**500°C 25 dpa Base Material**
α_l	0.603	0.541
α_{disp}	0.555	0.639
α_{nc}	0.288	0.354
S.S.S ($\Delta\sigma_{ss}$) MPa	-43	
$\Delta\boldsymbol{\sigma}_{\boldsymbol{y}}^{\boldsymbol{pred}}$	205	
$\Delta\boldsymbol{\sigma}_{\boldsymbol{y}}^{\boldsymbol{Meas}}$	-9	

Approach II – Coherent Nanoclusters

In this approach the same method as approach 1 is used to determine the strengthening coefficients of dislocation loops, and dispersoids, but a different approach is taken to determine nanoclusters. In approach 1 the nanoclusters were analyzed as incoherent in the matrix. In this approach an alternative equation expression developed by Tan and Busby [51] is used. This method evaluates the nanoclusters and assumes that they act coherently with the matrix. While it is not known if that is true, it is important to evaluate both conditions.

$$\alpha_{nc}^{coh} = \frac{0.816\gamma_{nc}\boldsymbol{d}}{\mu b^2\left(1-0.816\boldsymbol{d}\sqrt{\boldsymbol{N}\boldsymbol{d}}\right)} + 1.7\left(\frac{\boldsymbol{d}}{b}\right)^{1.5}\varepsilon^{1.5} + 0.0054\left(\frac{\boldsymbol{d}}{b}\right)^{0.275}\left(\frac{\Delta\mu}{\mu}\right)^{1.5} \quad (7)$$

where μ is the shear modulus (82.0 GPa), b is equal to the burgers vector (0.248 nm), and d and N are the nanocluster average diameter and number density, respectively. This equation for α_{nc}^{coh} depends on three unknown parameters: interfacial energy, γ_{nc} (J/m^2); lattice parameter mismatch between the cluster and matrix, ε; and shear modulus mismatch between the cluster and the matrix, $\Delta\mu$ (GPa). If we allow each of these unknowns to vary for each irradiation-induced cluster morphology, there are far more unknown variables than there are strengthening equations, rendering the system unsolvable via algebra. As a result, the approach applied here is to evaluate the range of values for which $\Delta\mu$, ε, and γ_{nc}, are valid (i.e. positive) to define a finite solution space. Varying these values gives a range of possible solutions for α_{nc} (Figure 2.3). Most importantly the α_{nc} fall within an extremely narrow band, suggesting that as long as reasonable ranges for these parameters are selected, they have little to no influence over the predicted yield strength.

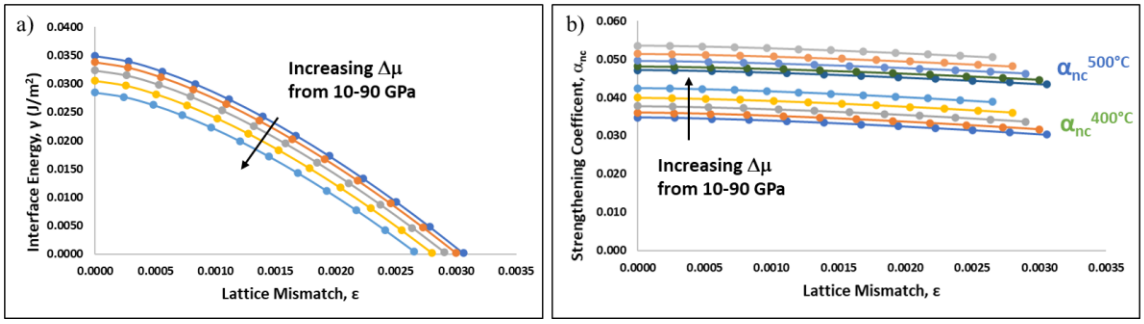

Figure 3.3. Solution space for: a.) γ_{nc}, ε, and $\Delta\mu$ for the base material using approach II with linear superposition. b.) α_{nc} for the base material at 400°C (green), and 500°C (blue).

Table 3.8. Summary of values for strengthening coefficients of loops (α_l), dispersoids (α_{disp}), and nanoclusters (α_{nc}) at temperatures of 400°C, and 500°C, and change in the solid solution strengthening. An average of the range of values for α_{nc} was used to predicted overall change in strengthening from irradiation temperatures using the linear superposition theorem compared to the measured strengthening values.

	MA956	
	400°C 25 dpa Base Material	**500°C 25 dpa Base Material**
α_l	0.603	0.541
α_{disp}	0.555	0.639
α_{nc}	0.030 – 0.042	0.043 – 0.054
S.S.S ($\Delta\sigma_{ss}$) MPa	-43	
$\Delta\boldsymbol{\sigma}_{\boldsymbol{y}}^{\boldsymbol{pred}}$	33.8	
$\Delta\boldsymbol{\sigma}_{\boldsymbol{y}}^{\boldsymbol{Meas}}$	-9	

Conclusion

In this study, alloy MA956 were presented in two different material conditions. One condition was the base metal that was irradiated at 1 and 25 dpa at 400°C, 450°C, and 500°C, and another was the stir zone irradiated at 1 and 25 dpa at 400°C, 450°C, and 500°C. Nanoindentation was conducted on all material conditions to measure the changing in hardness due to friction stir welding, and the different irradiation conditions. TEM, and APT was conducted in previous studies to determine micro-, and nano-structure changes in each specimen. The dispersed barrier hardening model was paired with the solution strengthening, and grain size dependence (Hall-Petch) models to determine the combined changes related to the microstructure, and microchemistry induced by different conditions. Based on the analysis the following conclusions are drawn:

1) In MA956, friction stir welding induces an increase in grain size, which is considered to contribute to 130 MPa softening in the material at all irradiation levels, when coupled with solid solution strengthening it is concluded that these features are the leading cause of decrease in strengthening of the material.
2) A model combining the dispersed barrier hardening and solid solution strengthening effects can reasonably predict the change in yield strength in irradiation conditions in the base material, and the stir zone from irradiation-induced evolution of the microstructure and microchemistry.
3) The approach to quantify the nanoclusters strengthening coefficient as coherent in the matrix using the 400°C 25 dpa to 500°C 25 dpa base material comparison, proves to be a more accurate estimation of the change in yield strength induced by these features.

Chapter 4: Conclusion

The ferritic-martensitic alloys, HT9, HCM12A, T91, and ODS alloy, MA956 are candidate materials for advanced nuclear reactors. The importance of understanding how these materials react to irradiation induced micro-, nano- structure features, and friction stir welding was accomplished in this study.

In chapter 2 of this study, a model combining the dispersed barrier hardening model and solid solution strengthening model was successfully used to reasonably predict the changes in yield strength of 3 separate alloys resulting in irradiation-induced evolution of the microstructure and microchemistry. Nanoindentation determined there was a decrease in yield strength in the high dose (100 dpa) compared to the low dose (2.4-3.0 dpa.) This was a result of the dissolution of nanoclusters into the matrix. It was also found that larger nanoclusters, such as in the HCM12A tend to have higher strengthening coefficients and are likely to have a larger combination of interfacial energy and lattice mismatch with the matrix.

In chapter 3 of this study, nanoindentation measured the base material compared to the stir zone of ODS alloy, MA956. It determined an average decrease in yield strength of 281 MPa across all irradiation conditions. Friction stir welding induces an increase in grain size compared to the base material and contributes to 130 MPa of softening at all irradiation conditions. When coupled with the solid solution strengthening model it can effectively predict the change in yield strength of the material due to friction stir welding. A model combing the dispersed barrier hardening model, and solid solution strengthening model can reasonably predict the change in yield strength in irradiation conditions of the base metal, and the stir zone from irradiation-induced evolution of the microstructure and microchemistry.

Finally, it was found in all four materials that nanoclusters must be modeled as coherent features in the matrix to reasonably predict the change in yield strength of the materials.

Literature Cited

[1] T. Allen, J. Busby, M. Meyer, D. Petti, Materials challenges for nuclear systems, Mater. Today. 13 (2010) 14–23. https://doi.org/10.1016/S1369-7021(10)70220-0.

[2] P. Yvon, F. Carré, Structural materials challenges for advanced reactor systems, J. Nucl. Mater. 385 (2009) 217–222. https://doi.org/10.1016/j.jnucmat.2008.11.026.

[3] D. Hull, D.J. Bacon, Introduction to Dislocations, Fifth, 2011. https://doi.org/10.1016/C2009-0-64358-0.

[4] A. Kareer, A. Prasitthipayong, D. Krumwiede, D.M. Collins, P. Hosemann, S.G. Roberts, An analytical method to extract irradiation hardening from nanoindentation hardness-depth curves, J. Nucl. Mater. 498 (2018) 274–281. https://doi.org/10.1016/j.jnucmat.2017.10.049.

[5] P. Hosemann, C. Shin, D. Kiener, Small scale mechanical testing of irradiated materials, J. Mater. Res. 30 (2015) 1231–1245. https://doi.org/10.1557/jmr.2015.26.

[6] C.D. Hardie, S.G. Roberts, A.J. Bushby, Understanding the effects of ion irradiation using nanoindentation techniques, J. Nucl. Mater. 462 (2015) 391–401. https://doi.org/10.1016/j.jnucmat.2014.11.066.

[7] P. Hosemann, C. Vieh, R.R. Greco, S. Kabra, J.A. Valdez, M.J. Cappiello, S.A. Maloy, Nanoindentation on ion irradiated steels, J. Nucl. Mater. 389 (2009) 239–247. https://doi.org/10.1016/j.jnucmat.2009.02.026.

[8] C. Deo, C. Tomé, R. Lebensohn, S. Maloy, Modeling and simulation of irradiation hardening in structural ferritic steels for advanced nuclear reactors, J. Nucl. Mater. 377 (2008) 136–140. https://doi.org/10.1016/j.jnucmat.2008.02.064.

[9] L. Tan, B.K. Kim, Y. Yang, K.G. Field, S. Gray, M. Li, Microstructural evolution of neutron-irradiated T91 and NF616 to ~4.3 dpa at 469 °C, J. Nucl. Mater. 493 (2017) 12–20. https://doi.org/10.1016/j.jnucmat.2017.05.041.

[10] C.K. Dolph, D.J. da Silva, M.J. Swenson, J.P. Wharry, Plastic zone size for nanoindentation of irradiated Fe—9%Cr ODS, J. Nucl. Mater. 481 (2016) 33–45. https://doi.org/10.1016/j.jnucmat.2016.08.033.

[11] S. Kotrechko, V. Dubinko, N. Stetsenko, D. Terentyev, X. He, M. Sorokin, Temperature dependence of irradiation hardening due to dislocation loops and precipitates in RPV steels and model alloys, J. Nucl. Mater. 464 (2015) 6–15. https://doi.org/10.1016/j.jnucmat.2015.04.014.

[12] R. Schäublin, A. Ramar, N. Baluc, V. de Castro, M.A. Monge, T. Leguey, N. Schmid, C. Bonjour, Microstructural development under irradiation in European ODS ferritic/martensitic steels, J. Nucl. Mater. 351 (2006) 247–260. https://doi.org/10.1016/j.jnucmat.2006.02.005.

[13] M.J. Swenson, J.P. Wharry, Nanocluster irradiation evolution in Fe-9%Cr ODS and ferritic-martensitic alloys, J. Nucl. Mater. 496 (2017) 24–40. https://doi.org/10.1016/j.jnucmat.2017.08.045.

[14] S.B. Adisa, R. Blair, M.J. Swenson, Comparison of microstructure evolution in Fe2+ or neutron-irradiated T91 at 500°C, Materialia. 12 (2020) 100770. https://doi.org/10.1016/j.mtla.2020.100770.

[15] J.F. Ziegler, M.D. Ziegler, J.P. Biersack, SRIM - The stopping and range of ions in matter (2010), Nucl. Instruments Methods Phys. Res. Sect. B Beam Interact. with Mater. Atoms. 268 (2010) 1818–1823. https://doi.org/10.1016/j.nimb.2010.02.091.

[16] M.J. Swenson, J.P. Wharry, TEM characterization of irradiated microstructure of Fe-9%Cr ODS and ferritic-martensitic alloys, J. Nucl. Mater. 502 (2018) 30–41. https://doi.org/10.1016/j.jnucmat.2018.01.062.

[17] J.M. Hyde, E.A. Marquis, K.B. Wilford, T.J. Williams, A sensitivity analysis of the maximum separation method for the characterisation of solute clusters, Ultramicroscopy. 111 (2011) 440–447. https://doi.org/10.1016/j.ultramic.2010.12.015.

[18] U. Kanders, K. Kanders, Strain hardening-softening oscillations induced by nanoindentation in bulk solids, (2016) 0–19. http://arxiv.org/abs/1609.09791.

[19] Y.F. Jia, Y.Y. Cui, F.Z. Xuan, F. Yang, Comparison between single loading-unloading indentation and continuous stiffness indentation, RSC Adv. 7 (2017) 35655–35665. https://doi.org/10.1039/c7ra06491h.

[20] W.C. Oliver, G.M. Pharr, An improved technique for determining hardness and elastic madulus using load and displacement, J Mater Res. 7 (1992) 1564–1583.

[21] P. Hosemann, D. Kiener, Y. Wang, S.A. Maloy, Issues to consider using nano indentation on shallow ion beam irradiated materials, J. Nucl. Mater. 425 (2012) 136–139. https://doi.org/10.1016/j.jnucmat.2011.11.070.

[22] D. Kramer, H. Huang, M. Kriese, J. Robach, J. Nelson, A. Wright, Yield Strength Predictions From the Plastic Zone Around Nanocontacts, Acta Mater. 47 (1999) 333–343.

[23] S.S. Chiang, The response of solids to elastic/plastic indentation. I. Stresses and residual stresses, J. Appl. Phys. 53 (1982) 298. https://doi.org/10.1063/1.329930.

[24] M. Yoshioka, Plastically deformed region around indentations on Si single crystal, J. Appl. Phys. 76 (1994) 7790. https://doi.org/10.1063/1.357957.

[25] C.K. Dolph, Plastic Deformation and Effective Strain Hardening Coefficient of Irradiated Fe-9wt%Cr ODS Alloy by Nanoindentation and TEM, Boise State University, 2015.

[26] Z. Huang, A. Harris, S.A. Maloy, P. Hosemann, Nanoindentation creep study on an ion beam irradiated oxide dispersion strengthened alloy, J. Nucl. Mater. 451 (2014) 162–167. https://doi.org/10.1016/j.jnucmat.2014.03.036.

[27] N. Gane, J.M. Cox, The micro-hardness of metals at very low loads, Philos. Mag. 22 (1970) 881–891. https://doi.org/10.1080/14786437008221059.

[28] C.F. Robertson, M.C. Fivel, Materials research, Science (80-.). 235 (1987) 9. https://doi.org/10.1126/science.235.4784.9.

[29] J.T. Busby, M.C. Hash, G.S. Was, The relationship between hardness and yield stress in irradiated austenitic and ferritic steels, J. Nucl. Mater. 336 (2005) 267–278. https://doi.org/10.1016/j.jnucmat.2004.09.024.

[30] A.C. Fischer-Cripps, Nanoindentation, Springer, New York, 2011.

[31] T.R. Allen, L. Tan, J. Gan, G. Gupta, G.S. Was, E.A. Kenik, S. Shutthanandan, S. Thevuthasan, Microstructural development in advanced ferritic – martensitic steel HCM12A, 351 (2006) 174–186. https://doi.org/10.1016/j.jnucmat.2006.02.014.

[32] J.P. Wharry, Z. Jiao, V. Shankar, J.T. Busby, G.S. Was, Radiation-induced segregation and phase stability in ferritic – martensitic alloy T 91, J. Nucl. Mater. 417 (2011) 140–144. https://doi.org/10.1016/j.jnucmat.2010.12.052.

[33] D.L. Krumwiede, T. Yamamoto, T.A. Saleh, S.A. Maloy, G.R. Odette, P. Hosemann, Direct comparison of nanoindentation and tensile test results on reactor-irradiated materials, J. Nucl. Mater. (2018). https://doi.org/10.1016/j.jnucmat.2018.03.021.

[34] J. Gao, K. Yabuuchi, A. Kimura, Ion-irradiation hardening and microstructural evolution in F82H and ferritic alloys, J. Nucl. Mater. 515 (2019) 294–302. https://doi.org/10.1016/j.jnucmat.2018.12.047.

[35] A. Zeman, L. Debarberis, J. Koc, Microstructural analysis of candidate steels pre-selected for new advanced reactor systems, 362 (2007) 259–267. https://doi.org/10.1016/j.jnucmat.2007.01.068.

[36] Y.F. Zhang, Q. Zhan, S. Ohnuki, A. Kimura, F.R. Wan, K. Yoshida, Y. Nagai, Radiation-hardening and nano-cluster formation in neutron- irradiated 9Cr e 2W low activation steels with different Si contents, J. Nucl. Mater. 517 (2019) 1–8. https://doi.org/10.1016/j.jnucmat.2019.01.053.

[37] T.P. Davis, M.A. Auger, C. Hofer, P.A.J. Bagot, M.P. Moody, D.E.J. Armstrong, Nanocluster evolution and mechanical properties of ion irradiated T91 ferritic-martensitic steel, J. Nucl. Mater. 548 (2021). https://doi.org/10.1016/j.jnucmat.2021.152842.

[38] S. Shu, P.B. Wells, N. Almirall, G.R. Odette, D.D. Morgan, Thermodynamics and kinetics of core-shell versus appendage co-precipitation morphologies: An example in the Fe-Cu-Mn-Ni-Si system, Acta Mater. 157 (2018) 298–306. https://doi.org/10.1016/j.actamat.2018.07.037.

[39] Q. Lu, W. Xu, S. Van Der Zwaag, Designing new corrosion resistant ferritic heat resistant steel based on optimal solid solution strengthening and minimisation of undesirable microstructural components, Comput. Mater. Sci. 84 (2014) 198–205. https://doi.org/10.1016/j.commatsci.2013.12.009.

[40] F.B. Pickering, Physical Metallurgy and the Design of Steels, Applied Science Publishers LTD, London, 1978.

[41] W.C. Leslie, Iron and its Dilute Solid Solutions, Metall. Trans. 3 (1972) 5–26.

[42] M.J. Swenson, C.K. Dolph, J.P. Wharry, The effects of oxide evolution on mechanical properties in proton- and neutron-irradiated Fe-9%Cr ODS steel, J. Nucl. Mater. 479 (2016) 426–435. https://doi.org/10.1016/j.jnucmat.2016.07.022.

[43] Z. Jiao, V. Shankar, G.S. Was, Phase stability in proton and heavy ion irradiated ferritic – martensitic alloys, J. Nucl. Mater. 419 (2011) 52–62. https://doi.org/10.1016/j.jnucmat.2011.08.020.

[44] G.R. Odette, G.E. Lucas, Embrittlement of Nuclear Reactor Pressure Vessels, (2001).

[45] P. Taylor, K. Fukuya, Journal of Nuclear Science and Technology Current understanding of radiation-induced degradation in light water reactor structural materials Current understanding of radiation-induced degradation in light water reactor structural materials, (2013) 37–41.

[46] J.E. Zelenty, J.E. Zelenty, Understanding thermally induced embrittlement in low copper RPV steels utilising atom probe tomography Understanding thermally induced embrittlement in low copper RPV steels utilising atom probe tomography, 0836 (2016). https://doi.org/10.1179/1743284714Y.0000000718.

[47] A. Seeger, J. Diehl, S. Mader, H. Rebstock, Work-hardening and work-softening of face-centred cubic metal crystals, Philos. Mag. 2 (1957) 323–350. https://doi.org/10.1080/14786435708243823.

[48] I. Kubena, B. Fournier, T. Kruml, Effect of microstructure on low cycle fatigue properties of ODS steels, J. Nucl. Mater. 424 (2012) 101–108. https://doi.org/10.1016/j.jnucmat.2012.02.011.

[49] G.S. WAS, G.S. Was, The Radiation Damage Event, 2017. https://doi.org/10.1007/978-1-4939-3438-6_1.

[50] G.R. Odette, G.E. Lucas, Radiation Effects and Defects in Solids : Incorporating Plasma Science and Plasma Technology Recent progress in understanding reactor pressure vessel steel embrittlement, n.d. https://doi.org/10.1080/10420159808229676.

[51] L. Tan, J.T. Busby, Formulating the strength factor α for improved predictability of radiation hardening, J. Nucl. Mater. 465 (2015) 724–730. https://doi.org/10.1016/j.jnucmat.2015.07.009.

[52] H. Oka, T. Tanno, S. Ohtsuka, Y. Yano, T. Uwaba, T. Kaito, M. Ohnuma, Effect of thermo-mechanical treatments on nano-structure of 9Cr-ODS steel, Nucl. Mater. Energy. 9 (2016) 346–352. https://doi.org/10.1016/j.nme.2016.10.007.

[53] S. Ukai, T. Okuda, M. Fujiwara, T. Kobayashi, S. Mizuta, H. Nakashima, Characterization of high temperature creep properties in recrystallized 12cr-ods ferritic steel claddings, J. Nucl. Sci. Technol. 39 (2002) 872–879. https://doi.org/10.1080/18811248.2002.9715271.

[54] J. Malaplate, F. Mompiou, J.L. Béchade, T. Van Den Berghe, M. Ratti, Creep behavior of ODS materials: A study of dislocations/precipitates interactions, J. Nucl. Mater. 417 (2011) 205–208. https://doi.org/10.1016/j.jnucmat.2010.12.059.

[55] M.J. Alinger, on the Formation Ang Stability of Nanoscale Percipatates in Ferritic Alloys During Processing and Hight Tempereture Servise .Pdf, (2004) 341.

[56] G. Gupta, Z. Jiao, A.N. Ham, J.T. Busby, G.S. Was, Microstructural evolution of proton irradiated T91, J. Nucl. Mater. 351 (2006) 162–173. https://doi.org/10.1016/j.jnucmat.2006.02.028.

[57] M. Matijasevic, A. Almazouzi, Effect of Cr on the mechanical properties and microstructure of Fe-Cr model alloys after n-irradiation, J. Nucl. Mater. 377 (2008) 147–154. https://doi.org/10.1016/j.jnucmat.2008.02.061.

[58] Z. Shang, J. Ding, C. Fan, D. Chen, J. Li, Y. Zhang, Y. Wang, H. Wang, X. Zhang, He ion irradiation response of a gradient T91 steel, Acta Mater. 196 (2020) 175–190. https://doi.org/10.1016/j.actamat.2020.06.019.

[59] K.G. Field, X. Hu, K.C. Littrell, Y. Yamamoto, L.L. Snead, Radiation tolerance of neutron-irradiated model Fe-Cr-Al alloys, J. Nucl. Mater. 465 (2015) 746–755. https://doi.org/10.1016/j.jnucmat.2015.06.023.

[60] F. Bergner, C. Pareige, M. Hernández-Mayoral, L. Malerba, C. Heintze, Application of a three-feature dispersed-barrier hardening model to neutron-irradiated Fe-Cr model alloys, J. Nucl. Mater. 448 (2014) 96–102. https://doi.org/10.1016/j.jnucmat.2014.01.024.

[61] B.W. Baker, T.R. McNelley, L.N. Brewer, Grain size and particle dispersion effects on the tensile behavior of friction stir welded MA956 oxide dispersion strengthened steel from low to elevated temperatures, Mater. Sci. Eng. A. 589 (2014) 217–227. https://doi.org/10.1016/j.msea.2013.09.092.

[62] B.W. Baker, K.E. Knipling, L.N. Brewer, Oxide Particle Growth During Friction Stir Welding of Fine Grain MA956 Oxide Dispersion-Strengthened Steel, Metall. Mater. Trans. E. 4 (2017) 1–12. https://doi.org/10.1007/s40553-016-0101-1.

Appendix A

The Young's Modulus as a function of indentation depth was used to determine the error in sampling the base metal, and the stir zone. The standard deviation was considered to understand if the indentation location was sampling more than one grain on the stir zone material.

Figure A: Summary of Young's Modulus as a function of indentation depth in MA956